Lead-Free NaNbO₃-Based Ceramics for Electrostatic Energy Storage Capacitors

Sairatun Nesa Soheli [1], Zhilun Lu [2,*], Dongyang Sun [1] and Islam Shyha [1]

[1] School of Computing, Engineering and Built Environment, Edinburgh Napier University, 10 Colinton Road, Edinburgh EH10 5DT, UK; sairatunnesa.soheli@napier.ac.uk (S.N.S.); d.sun@napier.ac.uk (D.S.); i.shyha@napier.ac.uk (I.S.)

[2] School of Chemical and Process Engineering, University of Leeds, Leeds LS2 JT, UK

* Correspondence: z.lu@leeds.ac.uk

Abstract: The burgeoning significance of antiferroelectric (AFE) materials, particularly as viable candidates for electrostatic energy storage capacitors in power electronics, has sparked substantial interest. Among these, lead-free sodium niobate (NaNbO₃) AFE materials are emerging as eco-friendly and promising alternatives to lead-based materials, which pose risks to human health and the environment, attributed to their superior recoverable energy density and dielectric breakdown strength. This review offers an insightful overview of the fundamental principles underlying antiferroelectricity and the applications of AFE materials. It underscores the recent advancements in lead-free NaNbO₃-based materials, focusing on their crystal structures, phase transitions, and innovative strategies devised to tailor their electrostatic energy storage performance. Finally, this review delineates the prevailing challenges and envisages future directions in the realm of NaNbO₃-based electrostatic energy storage capacitors, with the goal of fostering further advancements in this pivotal field.

Keywords: sodium niobate; antiferroelectric; lead-free material; energy storage capacitor

1. Introduction

In recent years, energy storage has emerged as a topic of significant interest because of the rapid advancement of technologically complex electronic devices and electrical power systems [1–3]. Electrostatic capacitors, electrochemical capacitors, batteries, and solid oxide fuel cells (SOFCs) are most of the technologies that can store energy, as shown in Figure 1. Electrostatic capacitors, also known as dielectric capacitors, offer many advantages over electrochemical capacitors, batteries, and SOFCs, including swift charging–discharging rates, ultrahigh power density, and excellent thermal stability, though they have a lower energy density. Among capacitors, electrochemical capacitors (e.g., supercapacitors) generally have a higher energy density compared to dielectric capacitors, primarily due to the significantly increased surface area of the electrodes. However, they also have a lower operating voltage, typically less than 3 V, exhibit significant leakage current (in mA), and are more expensive, costing around 9500 USD/kWh [4–7]. Therefore, dielectric capacitors are more suitable for low-cost, high-voltage, and large-scale applications [8].

When it involves analysing power and energy densities for energy storage devices (ESDs), the Ragone plot is an indispensable instrument. According to the evidence shown in Figure 1, it is not possible for a single ESD to concurrently possess both a high energy density and a high power density. It is possible to determine the application of each ESD based on its own characteristic time, which is determined by the energy-to-power ratio or charge/discharge rate of the device, as shown by the straight dashed lines in Figure 1 [9]. It is essential to remain conscious of the charge or discharge time in which external factors, such as the resistance of the load, might influence ESD encounters. As energy is stored in

a capacitor by the displacement of bound charged elements, capacitors have a higher charge or discharge rate and power density than batteries and SOFCs [10].
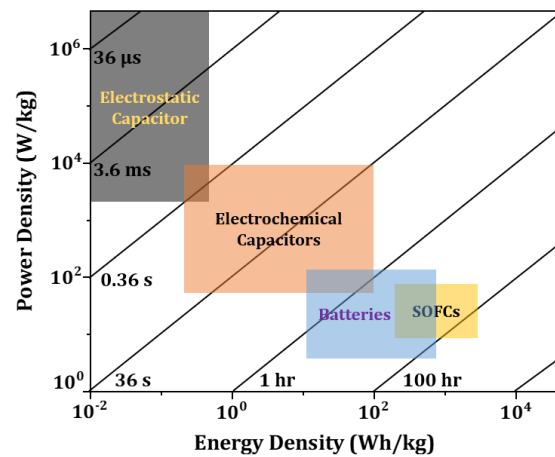
Figure 1. Ragone plot of various energy storage devices with characteristic times represented by straight dashed lines.

Dielectric capacitors are particularly useful for high-power/pulse-power systems due to their high charge or discharge rate, as indicated by their short characteristic time in Figure 1. This feature is also significant for effectively capturing energy from evanescent and intermittent renewable sources [11]. On the other hand, dielectric capacitors with enhanced energy densities offer significant benefits for a range of applications, including consumer electronics, commercial defibrillators, and pulsed power applications, due to their downsizing potential and easy integration [5,9,11–15]. Furthermore, increasing the energy density of dielectric capacitors to levels comparable with electrochemical capacitors or batteries [5] could significantly expand their use in energy storage, opening up a broader spectrum of applications.

Ceramic-based dielectric capacitors possess a rapid charge/discharge cycle and a high power density because of their ability to store energy via dipole moments as opposed to chemical reactions [10,16]. In addition, ceramics exhibit commendable mechanical properties and stability. These characteristics enable them to become fundamental elements of intermittent power systems. However, the application areas of ceramic capacitors are significantly limited because their integration and miniaturisation are impeded by their comparatively low recoverable energy storage density (W_{rec}) and energy storage efficiency (η). Therefore, the development of energy storage ceramics with superior efficacy is critical. Ceramic capacitors with high permittivity dielectrics are ideal for storing more energy due to their superior volumetric efficiency. These capacitors typically use ferroelectric (FE) materials, characterised by a spontaneous electric polarisation that can be modified with an external electric field [17]. In contrast, antiferroelectric (AFE) materials, while similar to FE materials, consist of adjacent dipoles in antiparallel orientations, leading to no net spontaneous polarisation [18,19]. AFE phases can undergo field-induced transitions to polar FE phases, leading to high polarisation at a high electric field. This opens up potential applications in energy storage, provided that the dielectric breakdown polarisation is high enough to induce the AFE-FE phase transition.

However, compared to FEs, AFEs are less commonly used due to the limited variety of AFE compounds and their less diverse functionalities [20,21]. Extensive research has been conducted on lead-based AFEs over the past decade, owing to their promising properties. Additionally, the phase stability of these materials can be easily adjusted through chemical substitution. The orthorhombic symmetry of the first lead-based AFE compound, $PbZrO_3$, was established by Sawaguchi et al. in 1951 [22]. Currently, over 40 types of AFE materials have been identified [23]. Among these, perovskite lead-based

compounds are particularly notable, including $PbHfO_3$ [24], (Pb, La) $(Zr, Ti)O_3$ [25], $(Pb, La)(Zr, Sn, Ti)O_3$ [26,27], $Pb_{0.97}La_{0.02}(Zr_{0.5}Sn_{0.43}Ti_{0.07})O_3$ [28], $Pb(In_{0.5}Nb_{0.5})O_3$ [29], and $Pb_{0.97}La_{0.02}(Zr, Sn, Ti)O_3$ [30].

It is worth noting that lead oxides and lead-containing compounds typically comprise about 70% of the raw material mass in certain applications [23]. Lead, a heavy metal, is highly toxic and can cause symptoms like abdominal pain, neurasthenia, anaemia, and toxic encephalopathy if it accumulates in the body beyond safe levels [31,32]. Recognising its danger to human and environmental health, many countries have regulated lead in electrical items [33,34]. This has spurred global research into lead-free dielectric materials, with notable progress in lead-free FEs [35–37], in contrast to the modest advances in lead-free AFEs [18,23,38].

As of the current date, $NaNbO_3$ and $AgNbO_3$ are recognised as leading examples of lead-free AFE materials. Figure 2 depicts the scholarly articles on lead-free AFE materials for energy storage published in Scopus-indexed journals from 2015 to 2024. Comparing the synthesis and processing of $NaNbO_3$ to $AgNbO_3$, it is observed that $NaNbO_3$ is more cost-effective, owing to its reliance on less expensive raw materials and the elimination of the need for a protective environment during the sintering process [39–41]. Despite the advantage of not requiring a protective atmosphere like oxygen, which is necessary for $AgNbO_3$, the higher sintering temperatures and the volatilisation of sodium at elevated temperatures present challenges in achieving high-quality $NaNbO_3$-based ceramics. Therefore, the hydrothermal method has been recently employed for the synthesis of both $NaNbO_3$ and $AgNbO_3$, leading to the production of high-quality ceramics [42,43].
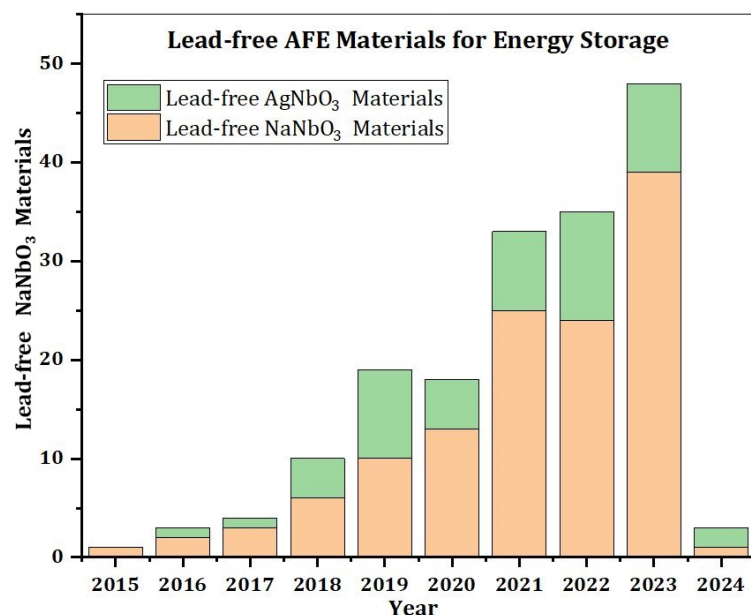
Figure 2. Publications on lead-free AFE materials for electrostatic energy storage (2015–2024).

The potential AFE properties of $NaNbO_3$ were initially identified in a publication in 1951 [44], coinciding with Kittel's proposal of the antiferroelectricity concept [45]. Recent advances have highlighted $NaNbO_3$ as a material of significant functional importance, particularly due to the discovery of unique AFE characteristics in some of its derived solid solutions [46,47]. These $NaNbO_3$-based solid solutions have drawn substantial interest for their ability to exhibit double loops and their relatively low density, estimated at 4.55 g/cm^3 [48]. Furthermore, the burgeoning scientific pursuit of innovative energy storage materials since 2015 has catalysed the development of compositionally altered $NaNbO_3$-based AFEs, characterised by their reversed field-induced phase transitions.

This review aims to provide a comprehensive summary of the latest advancements in lead-free $NaNbO_3$-based AFE ceramics for energy storage, a topic that has garnered considerable interest. Initially, it offers a succinct overview of the fundamental concepts and applications of AFE ceramics. It then delves into recent developments in lead-free $NaNbO_3$-based AFE materials, covering aspects such as crystal structures, phase transitions, chemical modifications (doping, solid solutions), and strategies devised to improve their energy storage capabilities [23,38,49,50]. Finally, the review addresses the outstanding challenges and future outlook in the study of $NaNbO_3$-based AFE ceramics and capacitors.

2. Fundamentals of AFEs

2.1. Definition of AFEs

AFE materials are closely related to FE materials but exhibit distinct characteristics. In FEs, the application of an external electric field aligns the inherent polarisation, resulting in a single polarisation hysteresis loop with a non-zero remanent polarisation (P_r). This residual polarisation persists even after the external field is removed, indicative of the FE nature.

In contrast, AFEs are characterised by a double polarisation hysteresis loop during field-induced phase transitions from the AFE to the FE state. Structurally, AFEs lack a macroscopic spontaneous polarisation, often described as inhibited FEs [51]. This inhibition is due to the equivalent antiparallel alignment of neighbouring dipoles, effectively cancelling out the macroscopic polarisation. This unique alignment and structural characteristic define AFEs as distinct yet related to traditional FE materials.

2.2. Applications of AFEs

In the early stages of their discovery, AFE materials were primarily regarded for actuation applications [52]. However, mechanical fractures often occurred due to the significant and abrupt strain changes during phase transitions, compromising the reliability of these actuators. At present, AFE materials are increasingly recognised for their potential in constructing high-energy-storage capacitors. Their potential to exhibit a higher electrostatic energy density than FEs and linear dielectrics makes them particularly suitable for high-density power applications in electronics, including DC-link and snubber capacitors [23,53–57].

The unique advantage of AFE materials in energy storage stems from the minimal energy differential between their anisotropic AFE phase and the field-induced FE phase. Under high electric fields, AFEs can transition to a highly polarised FE phase and revert to their original AFE state once the field is eliminated [50,58–60]. This property is in stark contrast to FEs and other dielectrics, which generally show a decrease in dielectric permittivity with increasing DC bias. Conversely, AFEs demonstrate an increase in permittivity at or just before the critical field that triggers the AFE-to-FE phase transition [61].

Furthermore, AFE materials are gaining attention for emerging applications in ultrafast neuromorphic computing [62], tunnel junctions [63], hybrid charge trap memories [64], ferroelectric random-access memories [65], and solid-state ferroic refrigerators [66]. The distinctive AFE properties in HfO_2-based materials are attributed to field-induced transitions between the polar orthorhombic phase ($Pca2_1$) [67] and the nonpolar tetragonal phase ($P4_2/nmc$), differing from the antiparallel dipole configuration found in materials like $PbZrO_3$ and $NaNbO_3$ [68]. Comprehensive discussions and evaluations of AFE materials are elaborated in other studies [38,69].

3. Dielectric Capacitors for Energy Storage

Dielectric materials are used in the middle layer between two conducting electrodes to construct a parallel-plate capacitor. The following equation is used to calculate the capacitance (C), representing a capacitor's ability to store energy:

$$C = \frac{\varepsilon_0 \, \varepsilon_r \, A}{d} \tag{1}$$

where ε_0 is the permittivity of free space (8.85×10^{-12} F/m), ε_r is the relative permittivity, A is the overlapping area of two electrodes, and d is the thickness of the dielectric layer.

When an external voltage is supplied, a charging process occurs, leading to the accumulation of charges at the electrodes. These charges, having opposite signs but equal magnitude, create an internal electric field. This field is directed opposite to the surrounding electric field. As more charges accumulate, the magnitude of this internal electric field within the system increases proportionally. The charging process completes when the internal electric field, induced by the collected charges (Q), equals the external electric field. The C of the capacitor is represented by Q/V. The amount of stored energy can be determined using the following equation:

$$W = \int_0^{Q_{max}} V dq \tag{2}$$

where Q_{max} is the maximum charge attained upon completion of the charging process, and dq denotes the incremental increase in charge.

Energy density (J) is a key metric for evaluating the energy storage performance of electrostatic capacitors. It quantifies the amount of energy stored relative to the capacitor's volume, providing a measure of how efficiently space is used for energy storage, as shown in Equation (3):

$$J = \frac{W}{Ad} = \frac{\int_0^{Q_{max}} V dq}{Ad} = \int_0^{D_{max}} E dD \tag{3}$$

where D is the electrical displacement within the dielectric layer. Consequently, D_{max} denotes the maximum electric displacement in the material when subjected to the highest applied electric field or dielectric breakdown strength, denoted as E_{max}.

In dielectrics with high permittivity, we often find that the electric displacement (D) closely approximates the polarisation (P). And D is calculated as the product of ε_0, ε_r, and E. Therefore, Equation (3) can be formulated as follows:

$$J = \int_0^{P_{max}} E dP = \int_0^{E_{max}} \varepsilon_0 \varepsilon_r \, E dE \tag{4}$$

Jaffe [13] states that the energy density can be determined by integrating the area that is bounded by the polarisation axis and the polarisation versus electric field $(P - E)$ curve. As shown in Figure 3a–c, the region shaded in blue represents the recovered energy density, denoted as J_{rec}, which is the energy released during the discharging process. Conversely, the orange region indicates the dissipated energy density (J_{loss}), attributable to losses within the dielectric material. The total energy density, J_{tot}, accumulated during the charging process equals the combined area of these two regions, reflecting their integral roles. J_{rec} is calculated using Equation (5):

$$J_{rec} = \int_{P_r}^{P_{max}} E dP \tag{5}$$

Furthermore, the ratio of recoverable energy density (J_{rec}) to the total energy storage density (J_{tot}) is equivalent to the energy efficiency (η), which can be expressed as:

$$\eta = \frac{J_{rec}}{J_{tot}} \times 100\% \tag{6}$$

where $J_{tot} = J_{rec} + J_{loss}$, and J_{loss} is the dissipated energy density, which is depicted as the orange region enclosed by the hysteresis loop.
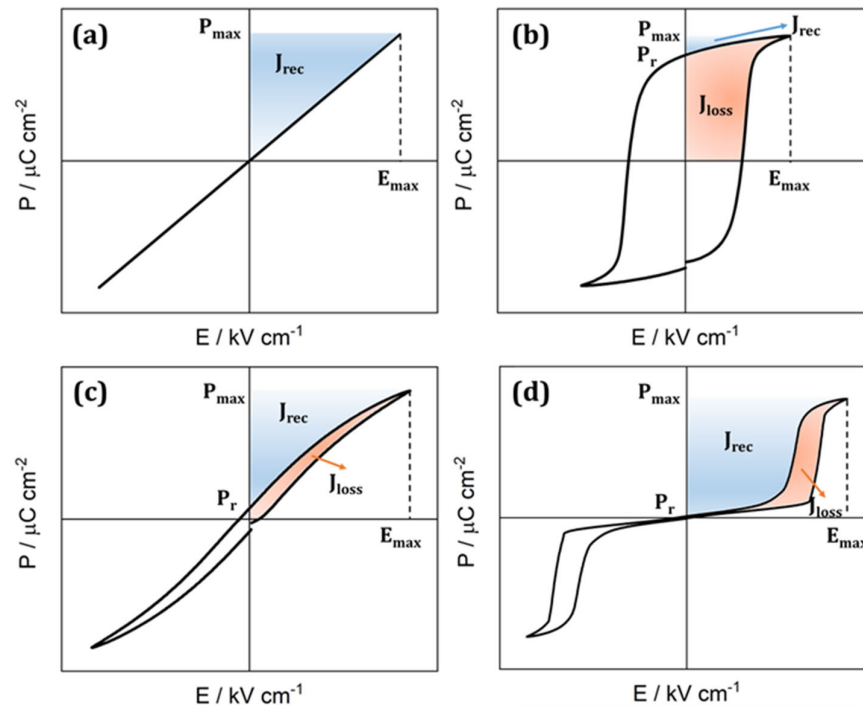
Figure 3. Schematic illustrations showing the polarisation versus electric field (P − E) curve: (**a**) linear dielectrics, (**b**) FEs, (**c**) relaxor ferroelectrics (RFEs), and (**d**) AFEs with the recoverable energy density (J_{rec}) and the dissipated energy density (J_{loss}) indicated in blue and orange areas, respectively.

It is important to note that nonlinear dielectric materials, such as FEs, relaxor ferroelectrics (RFEs), and AFEs, are known to exhibit J_{loss}. AFEs generally exhibit lower J_{loss} and higher E_{max} compared to FEs. According to Jaffe's theory, AFEs have the potential to significantly enhance energy storage capabilities, contingent upon resolving E_{max} challenges. Adequate E_{max} is crucial to enable the AFE-to-FE phase transition [13].

Figure 3d illustrates that AFEs often display hysteresis loops with a square recoverable energy area instead of a triangular one, a characteristic feature of AFEs [13]. The electric fields at which the AFE-FE transition begins and ends are referred to as the E_F and E_A threshold electric fields, respectively. As a result of their distinctive AFE-FE phase transitions, AFEs have a significant advantage in energy storage over linear dielectrics and FEs, owing to their enormous maximum polarisation (P_{max}) and minimal remnant polarisation (P_r) [70]. The residual polarisation in AFE ceramics is primarily a consequence of system defects and leakage currents. These can be reduced by employing appropriate doping strategies and microstructure optimisation. Modifying the critical phase transition electric field through chemical substitution is also feasible. Furthermore, the degradation resistance of ceramics is affected by various microstructural factors, including particle size, pore presence, secondary phases, and others. These aspects collectively influence the performance and reliability of AFE materials in energy storage applications [71–73].

4. Structural Characteristics of $NaNbO_3$-Based Ceramics

4.1. Crystal Structures of $NaNbO_3$

The structural complexity of $NaNbO_3$ arises from the displacement of Nb within its octahedral coordination and the tilting of the NbO_6 octahedra [74]. As illustrated in Figure 4 [69], at low temperatures (ranging from −100 °C to 360 °C), two phases of $NaNbO_3$ are observed to have very similar energy levels. These phases are designated as the P and Q phases, respectively. The P phase, identified as an AFE phase, possesses an orthorhombic space group Pbcm and is distinguished by antipolar distortions arising from the Nb-

O bonds. This phase features a superlattice structure of $\sqrt{2} \times \sqrt{2} \times 4$, relative to the aristo-type perovskite structure. The Q phase, an FE polar phase with the space group $P2_1ma$, features a $\sqrt{2} \times \sqrt{2} \times 2$ supercell and can be induced by applying an electric field. The coexistence of this polar Q phase and the antipolar P phase in $NaNbO_3$ complicates the analysis of double hysteresis loops, as evidenced in references [75–77].
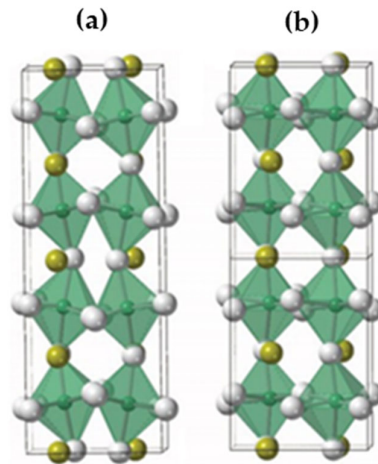
Figure 4. Crystal structures of $NaNbO_3$, with Na^+ in gold, Nb^{5+} in green, and O^{2-} in white: (**a**) the antipolar P phase and (**b**) the polar Q phase [69].

4.2. Phase Transitions in $NaNbO_3$

Seven distinct phases of $NaNbO_3$ can be observed as a function of temperature under ambient pressure, as shown in Figure 5. The high-temperature phase, manifesting at 639°C, adopts the aristo-type cubic perovskite structure with a cubic $Pm3m$ space group. Upon cooling, this structure transitions through a sequence of phases: tetragonal ($P4/mbm$), followed by four orthorhombic phases ($Ccmm$, $Pnmm$, $Pmnm$, and $Pbcm$), and ultimately to a rhombohedral ($R3c$) phase [23]. The identification of these phases is based on two primary factors: the displacement of Nb^{5+} ions from their octahedral centres and the tilting of oxygen octahedra. With heating, these tilts and displacements diminish, culminating in the restoration of the aristo-type cubic structure [74]. Notably, the rhombohedral N phase exhibits FE, whereas the orthorhombic P and R phases are AFE. All phases existing at temperatures above the R phase are paraelectric, displaying no spontaneous polarisation.

As opposed to $PbZrO_3$ or $AgNbO_3$ [78,79], which exhibit distinctive double polarisation hysteresis loops at elevated temperatures and ambient temperatures, respectively, pure $NaNbO_3$ undergoes an irreversible phase transition from the AFE state to the FE state [80,81]. Consequently, there is no known existence of steady double polarisation hysteresis loops in this $NaNbO_3$. Research by Cross and Nicholson [82], Ulinzheev et al. [83], and Miller et al. [84] into $NaNbO_3$ crystals has shown that applying electric fields, both parallel and perpendicular to the orthorhombic c axis, also known as the $[110]_{PC}$ direction, induces phase transitions. However, while a double hysteresis loop can initially be observed when a sufficiently strong electric field is applied perpendicular to the orthorhombic c axis [85], subsequent electrical cycles lead to instability, causing the loop to become indistinguishable from a typical FE loop. To date, there are no documented instances of double polarisation hysteresis loops in pure polycrystalline $NaNbO_3$ ceramics, highlighting a significant difference in the behaviour of $NaNbO_3$ compared to $PbZrO_3$ or $AgNbO_3$.
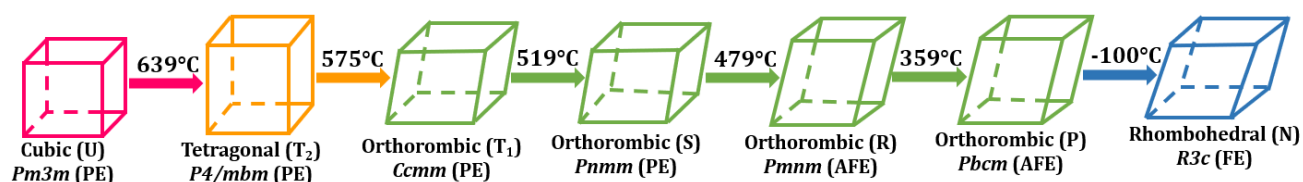
Figure 5. Temperature-dependent phase transitions in $NaNbO_3$.

Recent studies reveal that polycrystalline $NaNbO_3$ ceramics may display FE-type polarisation hysteresis loops [86], or display loops that remain unopened [87], as depicted in Figure 6. These phenomena are influenced by factors such as chemical composition [88], starting chemicals [89], and average grain size [90], which affect the stability between the AFE P and the FE Q phase. Koruza et al. [90] found that a phase transition from AFE to FE occurs in $NaNbO_3$ ceramics when the average grain size is below 0.27 mm, due to intragranular stresses.

(**a**)   (**b**)
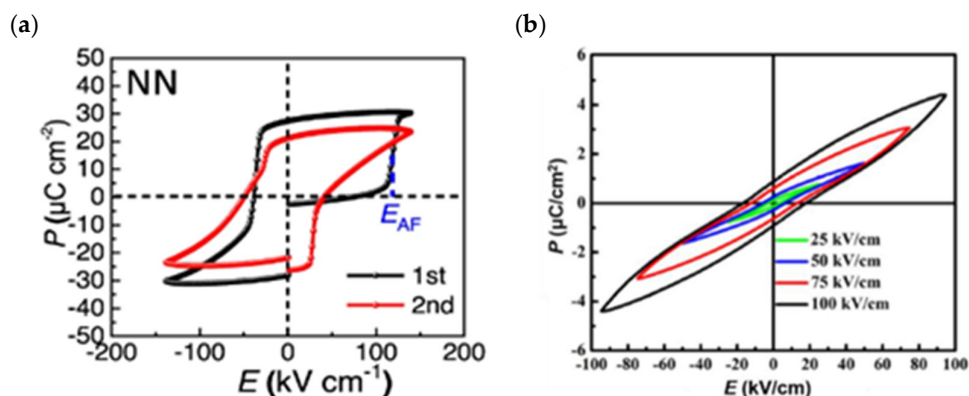
Figure 6. $P - E$ loops of $NaNbO_3$ bulk ceramics, as reported by (**a**) Luo et al. [86] and (**b**) Chao et al. [87].

Li et al. [89] observed that the fraction of P and Q phases varies with different Nb_2O_5 precursors, with a higher fraction from orthorhombic precursors, indicating stress-induced variations in phase amounts. Fan et al. [91] studied the impact of A site nonstoichiometry on phase stability, finding that all samples retained the AFE phase, unaffected by variations in Na content. M.-H. Zhang et al. [92] discovered that sintered $NaNbO_3$ ceramics, using orthorhombic Nb_2O_5 and with an average grain size of 8.9 mm, displayed a 100% AFE phase, highlighting the critical role of grain size in phase composition.

4.3. Phase Manipulation in $NaNbO_3$-Based Ceramics

Reproducing the initial experimental results on AFE in $NaNbO_3$ proved challenging, primarily due to variations in contaminant levels in the samples. These variations subtly affected the relative stability between the AFE and FE phases [82]. Structure analysis of $NaNbO_3$ was challenged by the nearly identical energy profiles of the P (AFE) and Q (FE) phases [77]. The isoenergetic relationship between these phases was confirmed through density functional theory (DFT) experiments [93]. The tolerance factor of $NaNbO_3$, approximately 0.967, prompted the investigation of solid solutions aimed at reducing this factor, thereby favoring the P phase stabilisation [94]. Experimental studies on $xCaZrO_3 - (1-x)NaNbO_3$ [95] and $xBiScO_3 - (1-x)NaNbO_3$ [94] solid solutions confirmed their AFE nature. Transmission electron microscopy (TEM) analysis of domain configurations revealed that reducing the tolerance factor systematically diminishes the Q phase, potentially stabilising a singular P phase. Although the precise mechanism remains partially understood, it is recognised that incommensurate phases facilitate the electric-field-

induced AFE to FE transition. These intermediate phases play a critical role, acting as a transitional bridge during polarisation reversal and the AFE to FE conversion in $NaNbO_3$ solid solutions [96]. Doping has been identified as a stabiliser for the incommensurate phase within the P phase region, a finding supported by analyses of polarisation current density and differential dielectric permittivity anomalies. This incommensurate phase is instrumental in the electric-field-induced polarisation reversal process, bridging the transition from AFE to FE states in $NaNbO_3$-based solid solutions [97].

Considerable effort has been devoted to chemically modified $NaNbO_3$ to achieve dual polarisation loops. Shimizu et al. proposed that the stability of the AFE order could be enhanced by simultaneously reducing the Goldschmidt tolerance factor and polarisability, taking into account the electronegativity differences in the new solid solutions [95]. A study investigated the impact of measurement frequency on the $P-E$ curves for $(0.94-x)NaNbO_3 - 0.06BaZrO_3 - xCaZrO_3$, with x = 0.04, as shown in Figure 7a [98]. Increasing frequencies led to a lag in AFE-FE phase transition and domain wall motion, decreasing their polarisation contribution and thus lowering the P_{max}. This was accompanied by increased polarisation hysteresis under an electric field, increasing E_F but decreasing E_A. In another system, $0.7NaNbO_3 - 0.3AgTaO_3$ [99], the $P-E$ loops, displayed in Figure 7b, exhibited distinct behaviour under varying electric fields. Notably, the application of high electric fields over 300 kV/cm resulted in reversible AFE-FE phase shifts, producing double $P-E$ loops with enhanced P_{max}.
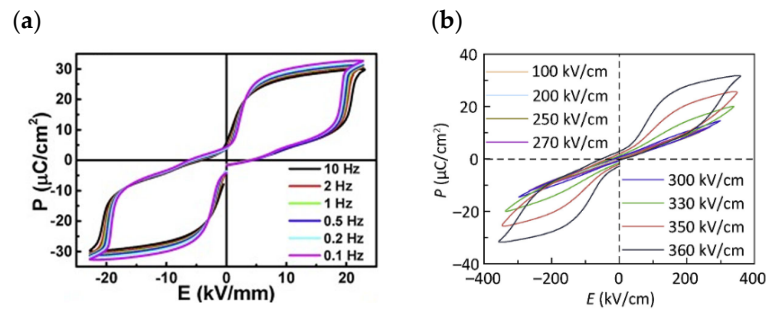
Figure 7. $P-E$ loops of (**a**) $0.9NaNbO_3 - 0.06BaZrO_3 - 0.04CaZrO_3$ [98], (**b**) $Na_{0.7}Ag_{0.3}Nb_{0.7}Ta_{0.3}O_3$ [99].

5. Tailoring Energy Storage Performance in $NaNbO_3$-Based Ceramics

5.1. Incorporation of MnO_2

In 2023, Zhang et al. reported a strategy to enhance the energy storage properties of $NaNbO_3$-based ceramics, specifically $0.95NaNbO_3 - 0.05SrSnO_3$ (NN5SS), through the incorporation of MnO_2. This approach, inspired by techniques used in lead-based materials, involves adding varying amounts of MnO_2 to serve as an electron trap (Equations (7) to (9)) [100]. Such a method has been previously documented to enhance the resistance of other perovskites [101,102]. Notably, it is recognised that Mn exhibits a preference for fewer oxidation states within perovskite structures [103]. The related reactions [100] are as follows:

$$Mn_{Nb}^x + e' = Mn'_{Nb} \qquad (7)$$

$$Mn'_{Nb} + e' = Mn''_{Nb} \qquad (8)$$

$$Mn''_{Nb} + e' = Mn'''_{Nb} \qquad (9)$$

The modification of $NaNbO_3$ by incorporating $SrSnO_3$ induces an augmentation in the local chemical disorder, thereby stabilising the AFE state [104]. Despite the tolerance factor for $NaNbO_3$ (NN, 0.965) and $0.95NaNbO_3 - 0.05SrSnO_3$ (NN5SS, 0.964) samples

being nearly identical, it is insufficient to solely rely on this metric for the stabilisation of AFE order without additional analysis. As shown in Figure 8a,b, NN exhibits FE behaviour, whereas NN5SS displays AFE-type double polarisation loops with a notable high remnant polarisation of $13.9 \, \mu C/cm^2$, influenced by leakage current. This phenomenon occurs as the $NaNbO_3 - SrSnO_3$ solid solution demonstrates $n - type$ conductivity due to a predominance of excess Sr over Na vacancies, in contrast to the $p - type$ conductivity observed in pure $NaNbO_3$ [105].
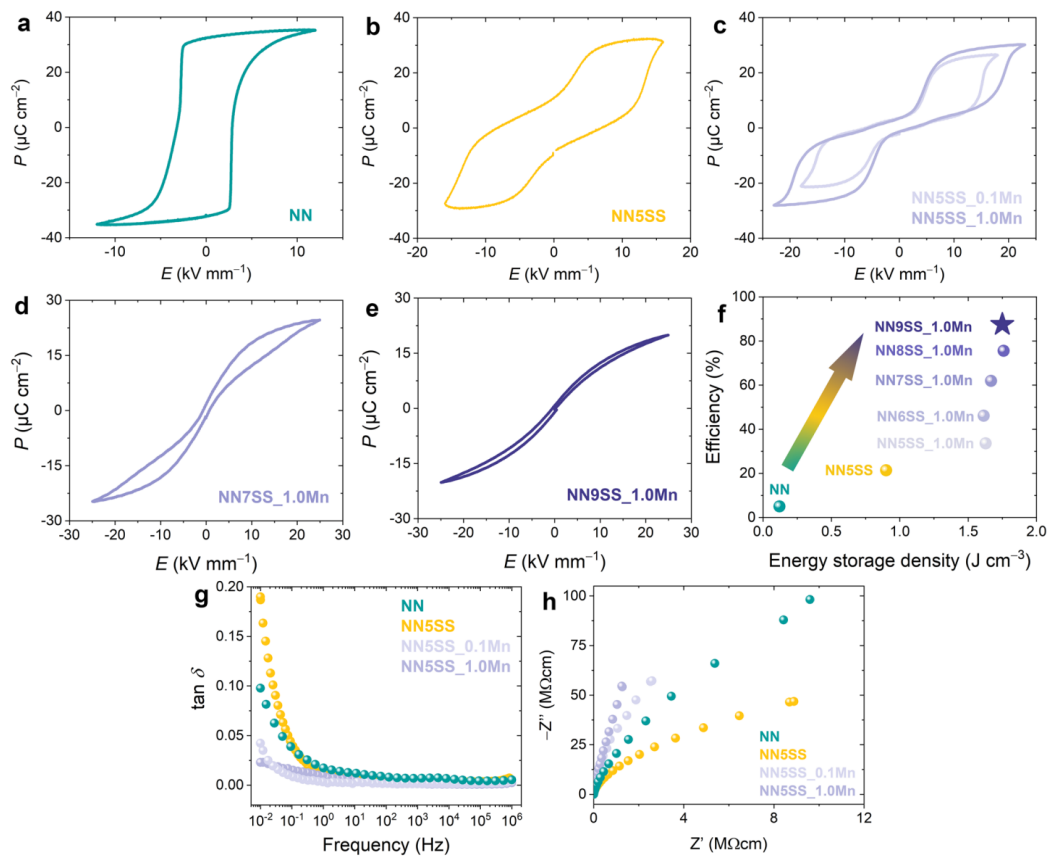
Figure 8. The second electric field cycle at 1 Hz produced $P - E$ loops for (**a**) NN, (**b**) NN5SS, (**c**) NN5SS_0.1 Mn and NN5SS_1.0Mn, (**d**) NN7SS_1.0Mn, and (**e**) NN9SS_1.0Mn; (**f**) recoverable energy storage density and efficiency; (**g**) $\tan\delta$ as a function of frequency; and (**h**) Nyquist plot of the NN, NN5SS, $NN5SS_{0.1Mn}$, and NN5SS_1.0Mn samples [100].

The inclusion of MnO_2 markedly reduces the dielectric loss, especially in the low-frequency region, as illustrated in Figure 8g, and concurrently elevates the resistance, as shown in Figure 8h. Consequently, the beneficial effect of the diminished quantity of charge carriers on the double hysteresis loops is evidenced in Figure 8c. Unlike the unaltered NN system, the modified samples exhibit a substantially lower remnant polarisation of $3.2 \, \mu C/cm^2$, representing a ten-fold reduction compared to the original system. No variation in phase transition behaviour is observed with an increase in Mn modification from 0.1 wt% to 1 wt%. The sole alteration is an increase in the critical field required to initiate the transition [100]. Energy storage efficiency improved from 21% in NN5SS to 33% in NN5SS_1.0Mn, yet remains low. Enhancing efficiency requires modifying polarisation loop shapes to be much slimmer, reducing hysteresis, and dispersing critical transition fields [106]. Figure 8d,e show that adjusting $SrSnO_3$ substitution levels while maintaining MnO_2 content boosts efficiency significantly from 33% to about 90% in NN9SS_1.0Mn,

as emphasised in Figure 8f. In summary, MnO_2 incorporation successfully suppresses mobile charge carriers, drastically lowers P_r, and increases material resistance.

5.2. Chemical Doping

Enhancing the energy storage properties of $NaNbO_3$-based ceramics through single-site doping at either the A-site or B-site is seldom reported. In 2018, Zhou et al. reported an approach to improve the energy storage capabilities of $NaNbO_3$-based ceramics by adding Bi_2O_3 [107]. This strategy potentially increases the E_{max} and reduces the P_r. Following Bi_2O_3 addition, the dielectric constant shows relaxor-like frequency dispersion near room temperature. The high E_{max} of ceramics is attributed to their dense microstructure and uniform chemical composition. When the E_{max} reaches $351 \, kV/cm$, the P_r nearly still zeroes. Moreover, the hybridisation interaction between the 6p orbitals of Bi^{3+} and the 2p orbitals of O^{2-} results in significant polarisation, with peak values exceeding $35 \, \mu C/cm^2$. Ceramics with a composition of $Na_{0.7}Bi_{0.1}NbO_3$ achieve an impressive energy storage density of $4.03 \, J/cm^3$ at $250 \, kV/cm$ and an energy storage efficiency of 85.4%, as demonstrated in Figure 9a,b [107].
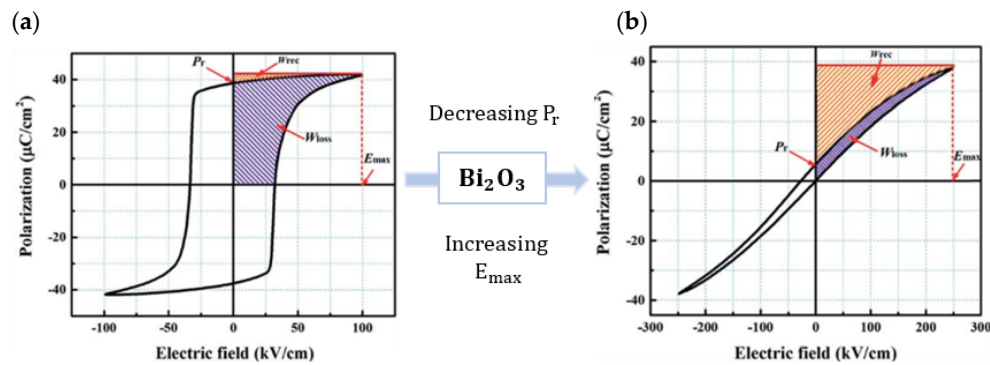
Figure 9. Schematic diagrams illustrating the enhancement of J_{rec} by adding Bi_2O_3 to $NaNbO_3$: (**a**) pure $NaNbO_3$ ceramics exhibit low J_{rec} due to high P_r and small E_{max}; (**b**) $Na_{1-3x}Bi_xNbO_3$ ceramics exhibit high J_{rec} due to low P_r and large E_{max} [107].

In 2022, L. Yang et al. significantly enhanced the energy storage properties of $NaNbO_3$-based ceramics through tantalum (Ta) doping. This modification reduced the dielectric loss and increased volume resistivity by substituting Nb^{5+} cations with Ta^{5+} cations at a concentration in the compound $(Na_{0.8}Bi_{0.1})(Nb_{0.9-x}Ta_xTi_{0.1})O_3$ (where $x = 0.15$) [108]. Such improvements have also been observed in various niobate ceramics, underscoring the broader applicability of this approach [109,110]. The improved volume resistivity of these ceramics contributes significantly to energy economy and E_{max} in energy storage applications [10]. The leakage current decreased after doping with 15% Ta^{5+} ions due to an increased bandgap, especially under high electric fields. Impedance spectroscopy revealed enhanced resistance both in the grains and at the grain boundaries, leading to an increase in E_{max} from $367 \, kV/cm$ to $469 \, kV/cm$. Remarkably, at $450 \, kV/cm$, the ceramics achieved a high recoverable energy density of $6.5 \, J/cm^3$ and an η of 94%, surpassing most $NaNbO_3$-based relaxor ceramics.

Additionally, these ceramic capacitors demonstrated excellent energy storage stability and performance across a wide temperature range ($-90 \, ℃$ to $150 \, ℃$) and over 10^5 cycles, as shown in Figure 10a,b [108]. The variation in $P - E$ loops between $-10 \, ℃$ and $0℃$ is attributed to adsorbed moisture on the sample interfaces, with a noticeable drop in P_{max} as the measurement temperature increases. These findings underscore the suitability of Ta-doped $NaNbO_3$-based ceramics for practical energy storage applications, thanks to their robust temperature stability and cycle-stable energy storage properties.
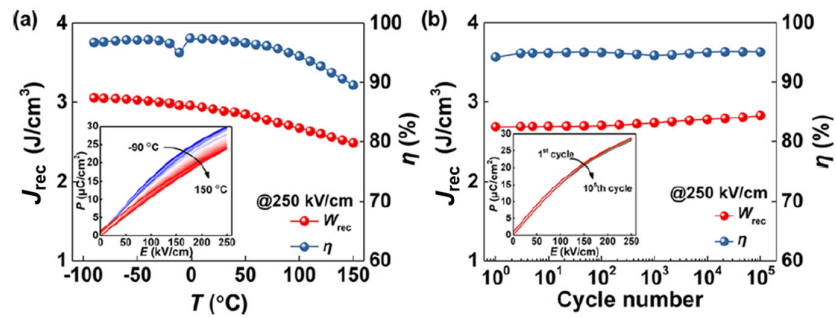
Figure 10. (**a**) The relationship between recoverable energy density and electric field at 250 kV/cm as a function of temperature is illustrated by the P − E loops obtained within an operating temperature range of −90℃ to 150℃. (**b**) The dependence of recoverable energy density and η on an electric field strength of 250 kV/cm is demonstrated through P − E loops from measurements conducted over several cycles, up to 10^5, at this field strength [108].

5.3. Improving Energy Storage Properties of NaNbO₃-Based Ceramics: Comprehensive Strategy Summaries

Recent literature has highlighted a variety of lead-free $NaNbO_3$-based materials notable for their high J_{rec}, as detailed in Table 1 with key sample preparation parameters such as thickness and electrode size. Reducing both thickness and electrode size effectively minimises the likelihood of detrimental defects, thereby increasing the E_{max}. This method facilitates achieving substantial energy storage properties under high electric fields (> 350 kV/cm), making it a preferred method among researchers striving for ultrahigh J_{rec} in materials of identical composition. Furthermore, J_{rec}, being directly correlated with the magnitude of the applied electric field, benefits from higher electric fields. However, to enable a more detailed comparison of energy storage performance across different systems, an analysis that normalises J_{rec} by the E_{max} is indispensable.

Table 1. Summary of energy storage properties of lead-free $NaNbO_3$-based materials with key sample preparation parameters.

$NaNbO_3$-Based Materials	E_{max} $\left(\frac{kV}{cm}\right)$	J_{rec} $\left(\frac{J}{cm^3}\right)$	$\frac{J_{rec}}{E_{max}}$ $\left(\frac{J}{kV\,cm^2}\right)$	η (%)	Thickness (mm)	Bulk/MLCC	Electrode and Size	Year	Ref.
$Na_{0.7}Ag_{0.3}Nb_{0.7}Ta_{0.3}O_3$	330	3.3	0.01	42.4	0.10	Bulk	Ag, 3.14 mm^2	2023	[99]
$0.8NaNbO_3 − 0.04CaZrO_3$-$0.16Bi_{0.5}Na_{0.5}TiO_3$	400	3.7	0.009	82.1	0.029	MLCC	Pt	2021	[111]
$0.88NaNbO_3 − 0.12Bi(Ni_{0.5}Zr_{0.5})O_3$	500	4.90	0.010	~72.0	0.15 ± 0.01	Bulk	Ag, 0.785 mm^2	2020	[112]
$0.85NaNbO_3 − 0.15Mg_{0.5}Hf_{0.5}O_3$	405	5.0	0.012	83.1	~0.11	Bulk	Au, ~3.14 mm^2	2023	[113]
$0.85NaNbO_3 − 0.15CaZrO_3$	680	5.4	0.008	82	~0.1	Bulk	Ag, ~3.14 mm^2	2023	[114]
$0.7NaNbO_3 − 0.3CaTiO_3$	560	5.52	0.010	83.3	0.1	Bulk	Au	2022	[115]
$0.95NaNbO_3 − 0.05Bi(Mg_{0.5}Sn_{0.5})O_3$	646	6.35	0.010	80.0	0.15 ± 0.01	Bulk	Ag, 0.785 mm^2	2022	[116]
$0.8NaNbO_3 − 0.2Bi(Ni_{0.5}Hf_{0.5})O_3$	380	6.45	0.017	82.72	-	Bulk	-	2024	[117]
$(Na_{0.8}Bi_{0.1})(Nb_{0.75}Ta_{0.15}Ti_{0.1})O_3$	450	6.5	0.014	94.0	0.08	Bulk	Au, 1.77 mm^2	2022	[108]

$Na_{0.7}Bi_{0.1}Nb_{0.9}Ta_{0.1}O_3$	560	6.68	0.012	90.5	0.15	Bulk	Au, 3.14 mm²	2022	[118]
$0.88NaNbO_3 - 0.12CaZrO_3$	650	8.56	0.013	82.0	~0.1	Bulk	Au, ~3.14 mm²	2022	[119]
$0.8(0.92NaNbO_3 - 0.08Bi(Ni_{0.5}Zr_{0.5})O_3) - 0.2(Bi_{0.5}Na_{0.5})0.7Sr_{0.3}TiO_3(0.2BNST)$	655	8.6	0.013	83.5	0.094	Bulk	3.14 mm²	2023	[120]
$0.68NaNbO_3 - 0.32(Bi_{0.5}Li_{0.5})TiO_3$	480	~8.73	~0.018	~80.1	0.12	Bulk	Ag, 3.14 mm²	2021	[121]
$0.85NaNbO_3 - 0.15Ca_{0.7}Sm_{0.2}TiO_3$	800	9.1	0.011	80.1	0.035	Bulk	Au, 3.14 mm²	2023	[122]
$0.76NaNbO_3 - 0.24(Bi_{0.5}Na_{0.5})TiO_3$	680	~12.2	~0.018	~69.0	0.15	Bulk	Ag, 7.07 mm²	2019	[123]
$0.67NaNbO_3 - 0.18(Bi_{0.5}Na_{0.5})TiO_3 - 0.15Bi(Mg_{0.5}Hf_{0.5})O_3$	700	12.65	0.018	88.5	0.0055	MLCC	70 Ag/30 Pd	2024	[124]
$NaNbO_3 - (Bi_{0.8}Sr_{0.2})(Fe_{0.9}Nb_{0.1})O_3$	983	16.5	0.017	83.3	0.06–0.08	Bulk	Ag, 0.785 mm²	2022	[125]
$0.9NaNbO_3 - 0.1BiFeO_3$	995	18.5	0.019	78.7	0.06–0.08	Bulk	Ag, 0.785 mm²	2021	[126]

It is worth noting that, compared to current lead-based materials with a remarkable J_{rec} of 11.18 J/cm³ in PbZrO₃-based bulk ceramics and an even larger J_{rec} of 12.6 J/cm³ in PbZrO₃-based multilayer ceramic capacitors (MLCCs) [127,128], lead-free $NaNbO_3$-based materials already exhibit a superior energy density exceeding 18 J/cm³, as shown in Table 1. To further enhance the J_{rec} of $NaNbO_3$-based ceramics, many strategies have been proposed, such as microstructure modification [129,130], electrical property tuning [82], and phase engineering [131,132].

5.3.1. Microstructure Modification

Examining the grain size of samples facilitates the microstructural tuning of sintered ceramics. Field-emission scanning electron microscopy (FE-SEM) images are indispensable for investigating these microstructures [42,133]. Figure 11a–e present the SEM images of polished samples of $0.955NaNbO_3 - 0.045La(Nb_{0.33}Mg_{0.67})O_3$ with varying additions of MnO_2 (0 wt%, 0.5 wt%, 1 wt%, 1.5 wt%, and 2 wt%) [134]. These images illustrate that all samples exhibit a dense packing with minimal porosity. The addition of MnO_2 resulted in a slight increase in grain size, attributed to the fluid phase facilitating atomic mobility. Notably, the particle size in all samples remained below 1 μm, contributing to an improvement in E_{max}.

Recent research has demonstrated that MLCC, which is constructed from a ceramic film with a layered structure [132], exhibits exceptional energy storage performance. This device is characterised by an ultrahigh J_{rec} and superior efficiency, in addition to exhibiting outstanding temperature stability and fatigue resistance [124].

Figure 12a–c present a comparison of $E_{test-max}$, J_{rec}, and η values for $0.82NaNbO_3 - 0.18(Bi_{0.5}Na_{0.5})TiO_3$ (NN–BNT), $0.67NaNbO_3 - 0.18(Bi_{0.5}Na_{0.5})TiO_3 - 0.15Bi(Mg_{0.5}Hf_{0.5})O_3$ (NN–BNT–15BMH) ceramic, and NN–BNT–15BMH MLCCs. The addition of BMH significantly enhances the $E_{test-max}$ in NN-BNT-15BMH ceramic samples. For MLCCs, reducing the dielectric layer thickness to 5.5 μm with NN–BNT–15BMH composition achieves an $E_{test-max}$ of 1100 kV/cm, nearly doubling the value observed in bulk ceramics. Furthermore, NN–BNT–15BMH MLCCs demonstrate an approximate 79.9% increase in J_{rec} compared to their ceramic counterparts [124].

Additionally, $NaNbO_3$ has been explored for its utility in energy storage materials when integrated into polymer matrices to form ceramic–polymer composites. Pan et al. discovered that high J_{rec} can be achieved in $NaNbO_3$/PVDF composites by optimising the composition of two-dimensional $NaNbO_3$ produced via the molten-salt method [135]. The composite exhibited a remarkable J_{rec} of 13.5 J/cm³ and a power density of

2.68 MW/cm^3 at an electric field of 4000 kV/cm, underscoring the potential of NaNbO$_3$ as a primary or supplementary component in energy storage applications.
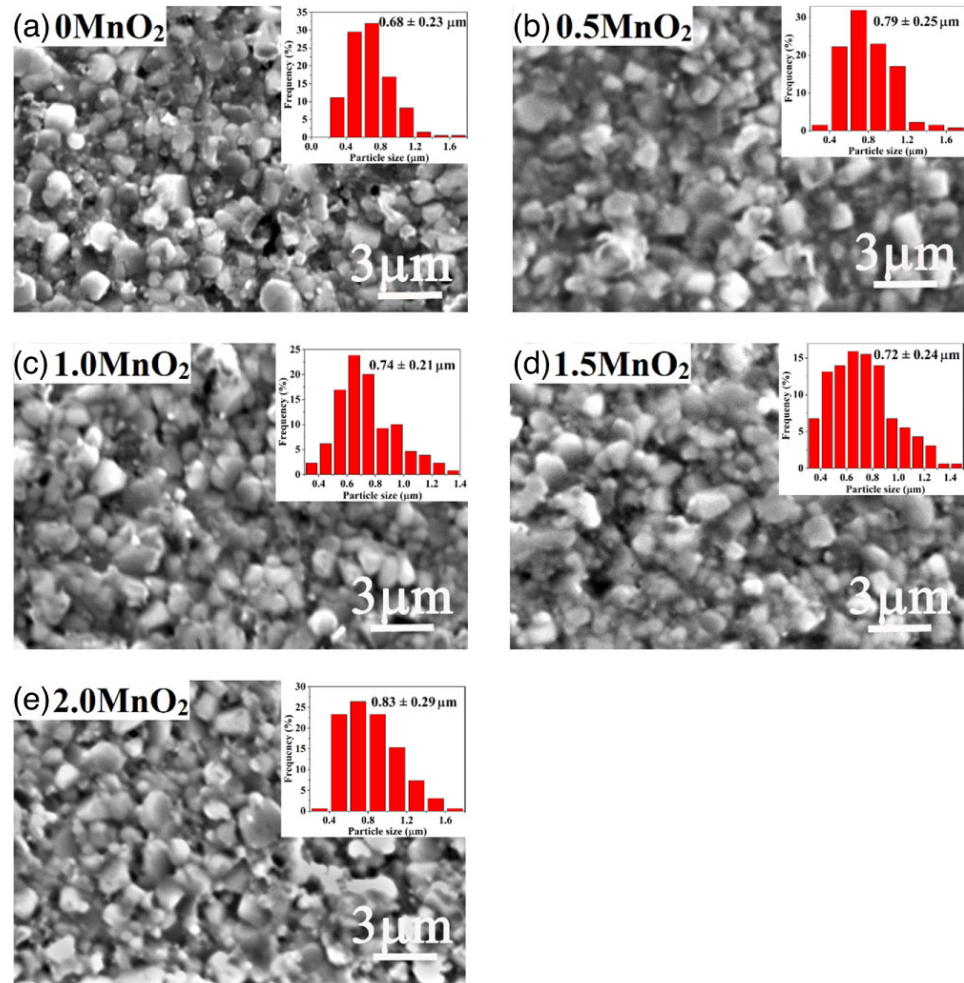
Figure 11. (**a–e**) SEM images of 0.955NaNbO$_3$ − 0.045La(Nb$_{0.33}$Mg$_{0.67}$)O$_3$ with varying additions of MnO$_2$: (**a**) 0 wt% MnO$_2$, (**b**) 0.5 wt% MnO$_2$, (**c**) 1.0 wt% MnO$_2$, (**d**) 1.5 wt% MnO$_2$, (**e**) 2.0 wt% MnO$_2$ [134].
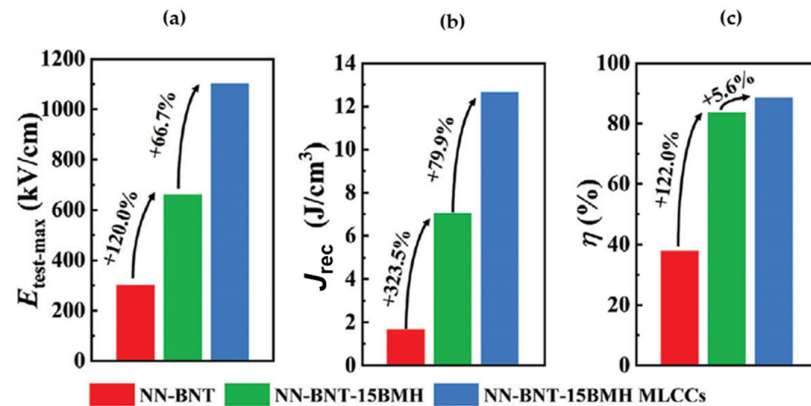
Figure 12. (**a**) Comparison between E$_{test−max}$, J$_{rec}$ and η of NN–BNT, (**b**) NN–BNT–15BMH ceramic, (**c**) NN–BNT–15BMH MLCCs [124].

5.3.2. Electrical Property Tuning

The tuning of electrical properties is directly linked to factors such as the band gap, conductivity, and electrical homogeneity. Lanfredi et al. conducted an investigation into the conductive properties of $NaNbO_3$ samples, which were synthesised using a wet chemical approach and subsequently analysed via impedance spectroscopy [136]. This analytical method facilitates the differentiation of grain boundary effects from the intrinsic properties of the grains themselves, thereby providing detailed insights into the resistivity, electrical homogeneity, and relaxation frequency [137,138]. Achieving a higher breakdown strength in $NaNbO_3$ necessitates the establishment of a substantial energy difference between the conduction and valence bands, commonly referred to as the band gap. A larger band gap is indicative of a lower likelihood of conductivity, underscoring the need for the material to possess strong insulating characteristics while maintaining minimal conductivity [82,139,140]. Enhancing electrical homogeneity has been demonstrated to significantly improve the E_{max} and, consequently, the J_{rec} in $BiFeO_3$-based ceramics [141,142]. Although $NaNbO_3$-based ceramics generally exhibit electrical homogeneity, as evidenced by complex impedance spectroscopy data presenting a singular semicircle in NN-BNT-15BMH (as shown in ref. [124]), it is noteworthy that grain refinement within these ceramics markedly increases the number of grain boundaries. This increase in grain boundaries leads to a pronounced rise in electrical resistance. The augmentation in resistance, in turn, enhances the insulating properties of the ceramics, contributing to an elevated E_{max}.

5.3.3. Phase Engineering

It has been reported that forming $NaNbO_3$-based solid solutions is a very promising method for phase engineering, which aims for high energy storage performance generally through inducing a relaxor state. This strategy significantly reduces P_r to achieve slimmer $P-E$ loops and enhances the E_{max}, leading to a higher J_{rec}.

As shown in Figure 13a,b, the compositions of $NaNbO_3$-based materials that employed this strategy exhibit relaxor-like characteristics, including broad dielectric anomalies with discernible frequency dispersion [125,130] and slim polarisation hysteresis loops [115,143,144]. These $NaNbO_3$-based solid solutions exhibit slim loops with remanence significantly reduced—up to ten-fold less—compared to pure $NaNbO_3$, heralding superior energy storage capabilities relative to conventional AFE materials due to the diminished electric-field-induced strain, especially in the absence of pronounced phase transitions that would compel volumetric changes under electric fields. Realising these advancements necessitates precise modifications to the local structure and defect chemistry.
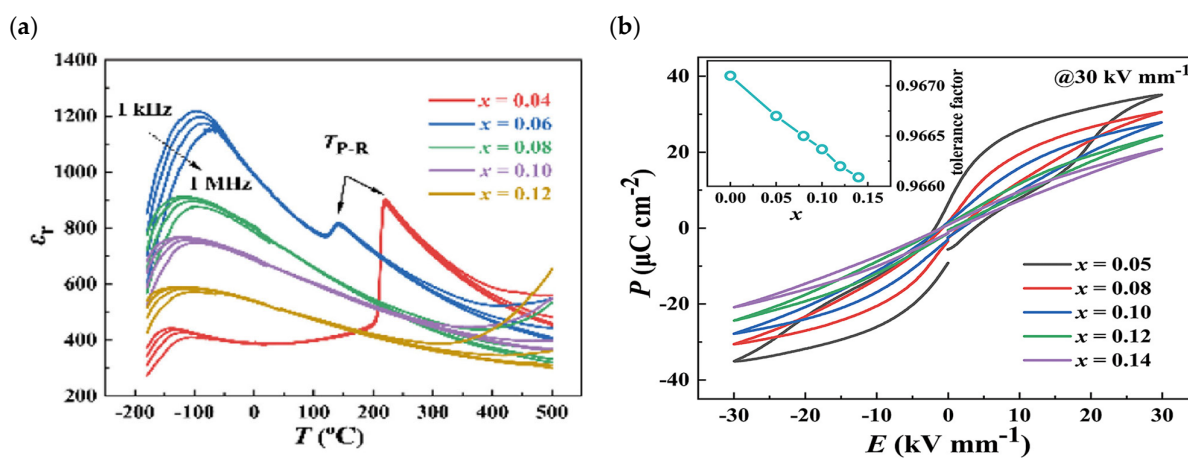
Figure 13. (**a**) Temperature-dependent measurements of dielectric permittivity at various frequencies for AFE samples of $(1-x)NaNbO_3 - x(Bi_{0.8}Sr_{0.2})(Fe_{0.9}Nb_{0.1})O_3$ [125]; (**b**) $P-E$ loops for $(1-x)NaNbO_3 - x(Bi_{0.8}Sr_{0.2})(Fe_{0.9}Nb_{0.1})O_3$ ceramics under 30 kV/mm at room temperature [125].

The phenomenon of relaxor behaviour has been identified as a contributor to facilitated polarisation rotation within ceramic materials [145], enhancing energy density through domain evaluation. External electric fields can reorient FE domains due to long-range dipole ordering [146–148]. High-performance piezoelectric materials benefit from phase barriers, which influence FE domain properties, reducing polarisation anisotropy and energy barriers through the creation of small domain sizes and high domain wall densities [149,150]. This reduction is primarily due to spontaneous polarisation (P_s) induced by lattice distortion, which is sensitive to external factors such as temperature, electric fields, ion substitution, and mechanical stresses. Moreover, nanoscale P_s fluctuations result in the formation of polar nanoregions (PNRs), exhibiting relaxor behaviour at the macroscopic level [151]. To enhance energy storage properties, the formation of PNRs has been identified as an effective strategy for increasing the energy efficiency of $NaNbO_3$-based ceramics [100,121]. The relaxor behaviour of the NN9SS_1.0Mn sample is illustrated in Figure 14a, with the presence of randomly distributed PNRs, each a few nm in size, further substantiated by high-resolution transmission electron microscopy (HRTEM) images in Figure 14b. Additionally, small-box modeling of the X-ray pair distribution functions (PDFs), shown in Figure 14c, reveals the local short-range structural order. These findings collectively underscore the emergence of a relaxor state, marked by the development of PNRs due to compositional and microstructural disorder. This relaxor state is instrumental in producing slimmer hysteresis loops and thereby enhancing energy storage efficiency [100].
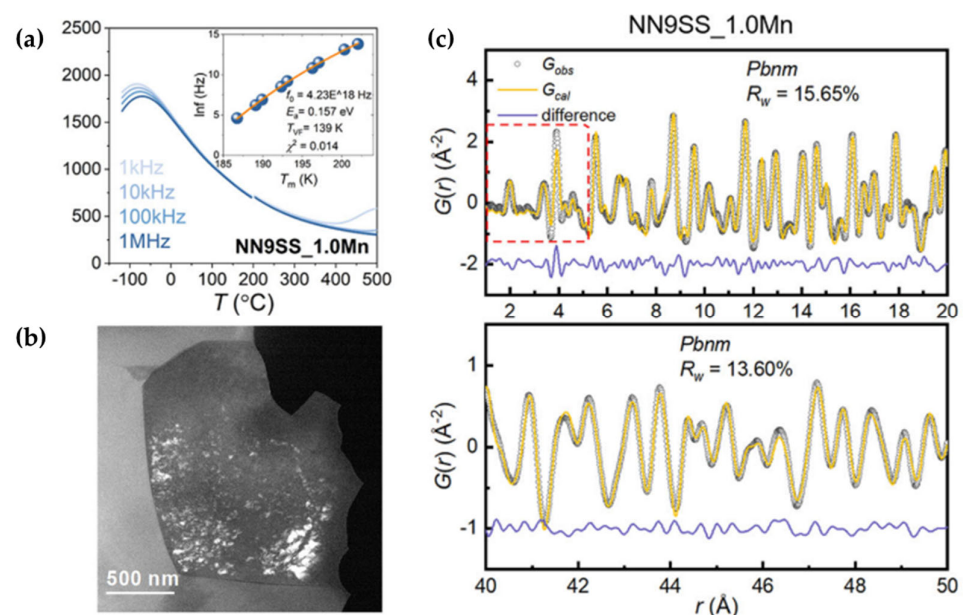
Figure 14. (**a**) Temperature-dependent dielectric permittivity; (**b**) domain morphology of the HRTEM images; (**c**) PDF analysis of relaxor states of the NN9SS_1.0Mn samples [100].

Importantly, $NaNbO_3$-based materials that display relaxorlike behaviours, occasionally termed "relaxor AFEs", present an ambiguous relationship with AFE behaviour, marked by a notable scarcity of superlattice reflection reports indicative of AFEs and the lack of current peaks in the $P − E$ loops that would signify field-induced transitions. A comprehensive analysis of the crystal structure through in situ high-energy synchrotron X-ray diffraction is anticipated to uncover the structural modifications correlating with functional property changes induced by electric field application. It is established that a reversible AFE–FE phase transition underpins the observed double polarisation hysteresis loops. Should phase transitions be unverifiable, leading to an absence of double $P − E$ loops, it may be posited that transitioning the initial state—whether FE or AFE—to a

relaxor state could enhance energy storage density, offering a more advantageous approach than categorising them strictly as "relaxor AFE" or "relaxor FE".

6. Summary and Outlook

Over the past decade, there has been significant progress in developing environmentally friendly, lead-free FEs in response to global environmental contamination and health risks. AFE perovskite oxides, distinguished by their intricate structures and a plethora of phase transitions, offer a compelling contrast to traditional FEs. However, despite their intriguing properties and potential applications, the exploration of AFEs, especially those exhibiting reversible AFE-FE transitions and lead-free variants such as $NaNbO_3$, remains nascent. A thorough grasp of crystal structure, phase structure, and microstructure is crucial for developing new AFE compositions. Given the increased complexity of AFE crystal structures compared to FEs, a multi-scale approach is essential to elucidate the fundamental mechanisms of antiferroelectricity.

The development of novel $NaNbO_3$-based AFE materials offers promising insights into the nuanced features of AFEs and their interaction with FE orders, highlighting the need for further theoretical research into the principles of antiferroelectricity in lead-free AFEs. Despite the focus on lead-based materials like $PbZrO_3$, the study of lead-free AFEs, such as $NaNbO_3$, is crucial for a deeper understanding of antiferroelectricity's origins. To finely tune the balance between AFE and FE orders in polycrystalline $NaNbO_3$, a better grasp of phase transition behaviours in single crystals is essential. This understanding could illuminate why the detection of double hysteresis loops is direction-dependent and whether textured ceramics could stabilise the AFE order [82]. However, research on field-induced phase transitions in high-quality alkaline niobate single crystals remains scarce [152].

The crystal structure and the dielectric properties of AFEs are comparable to those of FEs. Furthermore, the presence of variable degrees of competition between AFE and FE phases is almost ubiquitous in many compounds that are like them [153]. $NaNbO_3$ undergoes a convoluted series of phase changes as a function of temperature, which poses difficulties for the precise structural characterisation of the material. Even though various investigations have been conducted, there are still debates regarding this material. In recent years, significant advancements have been made in the development of chemically modified $NaNbO_3$ compositions that exhibit reversible phase transitions. Chemical modification is an effective method that can be utilised to adjust the phase stability of $NaNbO_3$ [154]. Despite these strides, the detailed mechanisms underpinning the structural changes in these materials are still only partially understood. Investigating the nucleation and growth of the field-induced FE phase, along with phase boundary migration during phase transitions in these new ceramics, is of keen interest. These studies are complicated by the processing sensitivities of the materials, including the hygroscopic nature of precursors, limited sintering windows, and the high vapour pressure of alkalis, necessitating further research on processing impacts.

The energy storage capabilities of $NaNbO_3$-based ceramics can be significantly augmented through the induction of relaxor-like characteristics, achieving a $P - E$ loop devoid of hysteresis and thereby maximising energy density. $NaNbO_3$-based materials already exhibit an J_{rec} exceeding 18 J/cm³, surpassing that of lead-based materials. This significant achievement indicates that lead-free $NaNbO_3$-based ceramics represent a viable alternative to lead-based materials in electrostatic energy storage capacitors. With strategic compositional adjustments and advancements in synthesis techniques, there is strong potential for further enhancing the J_{rec} of $NaNbO_3$-based ceramics. Despite these advancements, considerable challenges persist in resolving fundamental scientific inquiries. These include establishing criteria for the stability assessment between FE and AFE states, tailoring energy states for optimal performance, and precisely delineating the characteristics inherent to AFE materials. Nonetheless, the continuous evolution of experimental and theoretical research methodologies harbours a promising outlook for the development of lead-free AFE materials endowed with superior energy storage capacities.

In the realm of energy storage capacitors, MLCCs boasting higher capacity and compactness are pivotal for practical device applications. To address the demands of high-voltage power electronics, development is required not only in dielectric materials but also in the substitution of expensive electrodes like Ag and Pt with more cost-effective alternatives such as Cu and Ni, ensuring compatibility. Thus, a significant challenge lies in reducing the sintering temperature of $NaNbO_3$-based ceramics without compromising their properties. Additionally, the focus on temperature stability and long-term reliability will be crucial for advancing $NaNbO_3$-based electrostatic energy storage capacitors.

Institutional Review Board Statement: Not applicable.

Informed Consent Statement: Not applicable.

Data Availability Statement: No new data were created or analyzed in this study.

Conflicts of Interest: The authors declare no conflict of interest.

References

1. Wang, G.; Lu, Z.; Li, Y.; Li, L.; Ji, H.; Feteira, A.; Zhou, D.; Wang, D.; Zhang, S.; Reaney, I.M. Electroceramics for high-energy density capacitors: Current status and future perspectives. *Chem. Rev.* **2021**, *121*, 6124–6172.
2. Lin, J.; Cao, Y.; Zhu, K.; Yan, F.; Shi, C.; Bai, H.; Ge, G.; Yang, J.; Yang, W.; Li, G. Ultrahigh energy harvesting properties in temperature-insensitive eco-friendly high-performance KNN-based textured ceramics. *J. Mater. Chem. A* **2022**, *10*, 7978–7988.
3. Yan, F.; Bai, H.; Ge, G.; Lin, J.; Zhu, K.; Li, G.; Qian, J.; Shen, B.; Zhai, J.; Liu, Z. Boosting Energy Storage Performance of Lead-Free Ceramics via Layered Structure Optimization Strategy. *Small* **2022**, *18*, 2202575.
4. Kusko, A.; Dedad, J. Short-term, long-term, energy storage methods for standby electric power systems. In Proceedings of the Fourtieth IAS Annual Meeting. Conference Record of the 2005 Industry Applications Conference, Hong Kong, China, 2–6 October 2005.; pp. 2672–2678.
5. Yao, K.; Chen, S.; Rahimabady, M.; Mirshekarloo, M.S.; Yu, S.; Tay, F.E.H.; Sritharan, T.; Lu, L. Nonlinear dielectric thin films for high-power electric storage with energy density comparable with electrochemical supercapacitors. *IEEE Trans. Ultrason. Ferroelectr. Freq. Control* **2011**, *58*, 1968–1974.
6. Gomez Vidales, A.; Sridhar, D.; Meunier, J.-L.; Omanovic, S. Nickel oxide on directly grown carbon nanofibers for energy storage applications. *J. Appl. Electrochem.* **2020**, *50*, 1217–1229.
7. Gomez Vidales, A.; Kim, J.; Omanovic, S. $Ni_{0.6−x}Mo_{0.4−x}Ir_x$-oxide as an electrode material for supercapacitors: Investigation of the influence of iridium content on the charge storage/delivery. *J. Solid State Electrochem.* **2019**, *23*, 2129–2139.
8. Bhalerao, S.; Ambhore, N.; Kadam, M. Polymer matrix composite in high voltage applications: A review. *Biointerface Res. Appl. Chem* **2022**, *12*, 8343–8352.
9. Christen, T.; Carlen, M.W. Theory of Ragone plots. *J. Power Sources* **2000**, *91*, 210–216.
10. Yang, L.; Kong, X.; Li, F.; Hao, H.; Cheng, Z.; Liu, H.; Li, J.-F.; Zhang, S. Perovskite lead-free dielectrics for energy storage applications. *Prog. Mater. Sci.* **2019**, *102*, 72–108. https://doi.org/10.1016/j.pmatsci.2018.12.005.
11. Sherrill, S.A.; Banerjee, P.; Rubloff, G.W.; Lee, S.B. High to ultra-high power electrical energy storage. *Phys. Chem. Chem. Phys.* **2011**, *13*, 20714–20723.
12. Whittingham, M.S. Materials challenges facing electrical energy storage. *Mrs Bull.* **2008**, *33*, 411–419.
13. Jaffe, B. Antiferroelectric ceramics with field-enforced transitions: A new nonlinear circuit element. *Proc. IRE* **1961**, *49*, 1264–1267.
14. Ulrich, R.; Schaper, L.; Nelms, D.; Leftwich, M. Comparison of paraeletric and ferroelectric materials for applications as dielectrics in thin film integrated capacitors. *Int. J. Microcircuits Electron. Packag.* **2000**, *23*, 172–181.
15. Park, S.-E.; Shrout, T.R. Ultrahigh strain and piezoelectric behavior in relaxor based ferroelectric single crystals. *J. Appl. Phys.* **1997**, *82*, 1804–1811.
16. Love, G.R. Energy storage in ceramic dielectrics. *J. Am. Ceram. Soc.* **1990**, *73*, 323–328.
17. Krohns, S.; Lunkenheimer, P. Ferroelectric polarization in multiferroics. *Phys. Sci. Rev.* **2019**, *4*, 20190015.
18. Gao, J.; Li, Q.; Zhang, S.; Li, J.-F. Lead-free antiferroelectric $AgNbO_3$: Phase transitions and structure engineering for dielectric energy storage applications. *J. Appl. Phys.* **2020**, *128*, 070903.
19. Tolédano, P.; Guennou, M. Theory of antiferroelectric phase transitions. *Phys. Rev. B* **2016**, *94*, 014107.

20. Li, P.-F.; Liao, W.-Q.; Tang, Y.-Y.; Ye, H.-Y.; Zhang, Y.; Xiong, R.-G. Unprecedented ferroelectric–antiferroelectric–paraelectric phase transitions discovered in an organic–inorganic hybrid perovskite. *J. Am. Chem. Soc.* **2017**, *139*, 8752–8757.

21. Xu, C.; Liu, Z.; Chen, X.; Yan, S.; Cao, F.; Dong, X.; Wang, G. Pulse discharge properties of PLZST antiferroelectric ceramics compared with ferroelectric and linear dielectrics. *AIP Adv.* **2017**, *7*, 115108.

22. Sawaguchi, E.; Maniwa, H.; Hoshino, S. Antiferroelectric structure of lead zirconate. *Phys. Rev.* **1951**, *83*, 1078.

23. Yang, D.; Gao, J.; Shu, L.; Liu, Y.-X.; Yu, J.; Zhang, Y.; Wang, X.; Zhang, B.-P.; Li, J.-F. Lead-free antiferroelectric niobates $AgNbO_3$ and $NaNbO_3$ for energy storage applications. *J. Mater. Chem. A* **2020**, *8*, 23724–23737.

24. Shirane, G.; Pepinsky, R. Phase Transitions in Antiferroelectric $PbHfO_3$. *Phys. Rev.* **1953**, *91*, 812.

25. Haertling, G. Improved hot-pressed electrooptic ceramics in the (Pb, La)(Zr, Ti) O_3 system. *J. Am. Ceram. Soc.* **1971**, *54*, 303–309.

26. Yang, Y.; Liu, P.; Zhang, Y.; Kandula, K.R.; Xu, J.; Zhang, G.; Jiang, S. Low electric-field-induced strain and high energy storage efficiency in (Pb, Ba, La)(Zr, Sn, Ti) O_3 antiferroelectric ceramics through regulating the content of La. *Ceram. Int.* **2020**, *46*, 18106–18113.

27. Dan, Y.; Zou, K.; Chen, G.; Yu, Y.; Zhang, Y.; Zhang, Q.; Lu, Y.; Zhang, Q.; He, Y. Superior energy-storage properties in (Pb, La)(Zr, Sn, Ti) O_3 antiferroelectric ceramics with appropriate La content. *Ceram. Int.* **2019**, *45*, 11375–11381.

28. Xu, H.; Dan, Y.; Zou, K.; Chen, G.; Zhang, Q.; Lu, Y.; He, Y. Superior energy storage performance in $Pb_{0.97}La_{0.02}(Zr_{0.50}Sn_{0.43}Ti_{0.07})O_3$ antiferroelectric ceramics. *J. Mater. Res. Technol.* **2019**, *8*, 3291–3296.

29. Isupov, V. Ferroelectric and antiferroelectric perovskites $PbB'_{0.5}B''_{0.5}O_3$. *Ferroelectrics* **2003**, *289*, 131–195.

30. Hao, X.; Zhao, Y.; Zhang, Q. Phase structure tuned electrocaloric effect and pyroelectric energy harvesting performance of $(Pb_{0.97}La_{0.02})(Zr, Sn, Ti) O_3$ antiferroelectric thick films. *J. Phys. Chem. C* **2015**, *119*, 18877–18885.

31. O'Connor, D.; Hou, D.; Ye, J.; Zhang, Y.; Ok, Y.S.; Song, Y.; Coulon, F.; Peng, T.; Tian, L. Lead-based paint remains a major public health concern: A critical review of global production, trade, use, exposure, health risk, and implications. *Environ. Int.* **2018**, *121*, 85–101.

32. Kumar, A.; Kumar, A.; MMS, C.-P.; Chaturvedi, A.K.; Shabnam, A.A.; Subrahmanyam, G.; Mondal, R.; Gupta, D.K.; Malyan, S.K.; Kumar, S.S. Lead toxicity: Health hazards, influence on food chain, and sustainable remediation approaches. *Int. J. Environ. Res. Public Health* **2020**, *17*, 2179.

33. Wang, R.; Xu, Z. Recycling of non-metallic fractions from waste electrical and electronic equipment (WEEE): A review. *Waste Manag.* **2014**, *34*, 1455–1469.

34. Goosey, E.; Goosey, M. The materials of waste electrical and electronic equipment. In *Waste Electrical and Electronic Equipment (WEEE) Handbook*; Elsevier: Amsterdam, The Netherlands, 2019; pp. 231–262.

35. Sun, Z.; Wang, Z.; Tian, Y.; Wang, G.; Wang, W.; Yang, M.; Wang, X.; Zhang, F.; Pu, Y. Progress, outlook, and challenges in lead-free energy-storage ferroelectrics. *Adv. Electron. Mater.* **2020**, *6*, 1900698.

36. Kumari, P.; Rai, R.; Sharma, S.; Shandilya, M.; Tiwari, A. State-of-the-art of lead free ferroelectrics: A critical review. *Adv. Mater. Lett* **2015**, *6*, 453–484.

37. Zhang, S.; Malič, B.; Li, J.-F.; Rödel, J. Lead-free ferroelectric materials: Prospective applications. *J. Mater. Res.* **2021**, *36*, 985–995.

38. Liu, Z.; Lu, T.; Ye, J.; Wang, G.; Dong, X.; Withers, R.; Liu, Y. Antiferroelectrics for energy storage applications: A review. *Adv. Mater. Technol.* **2018**, *3*, 1800111.

39. Gao, J.; Zhang, Y.; Zhao, L.; Lee, K.-Y.; Liu, Q.; Studer, A.; Hinterstein, M.; Zhang, S.; Li, J.-F. Enhanced antiferroelectric phase stability in La-doped $AgNbO_3$: Perspectives from the microstructure to energy storage properties. *J. Mater. Chem. A* **2019**, *7*, 2225–2232.

40. Gao, J.; Liu, Q.; Dong, J.; Wang, X.; Zhang, S.; Li, J.-F. Local structure heterogeneity in Sm-doped $AgNbO_3$ for improved energy-storage performance. *ACS Appl. Mater. Interfaces* **2020**, *12*, 6097–6104.

41. Gao, J.; Zhao, L.; Liu, Q.; Wang, X.; Zhang, S.; Li, J.F. Antiferroelectric-ferroelectric phase transition in lead-free $AgNbO_3$ ceramics for energy storage applications. *J. Am. Ceram. Soc.* **2018**, *101*, 5443–5450.

42. Lu, Y.; Karaki, T.; Fujii, T. Hydrothermal synthesis of plate-like sodium niobate particles. *Ceram. Int.* **2015**, *41*, S174–S179.

43. Wang, J.; Wan, X.; Rao, Y.; Zhao, L.; Zhu, K. Hydrothermal synthesized $AgNbO_3$ powders: Leading to greatly improved electric breakdown strength in ceramics. *J. Eur. Ceram. Soc.* **2020**, *40*, 5589–5596. https://doi.org/10.1016/j.jeurceramsoc.2020.06.031.

44. Vousden, P. The structure of ferroelectric sodium niobate at room temperature. *Acta Crystallogr.* **1951**, *4*, 545–551.

45. Kittel, C. Theory of antiferroelectric crystals. *Phys. Rev.* **1951**, *82*, 729.

46. Torres-Pardo, A.; Jiménez, R.; García-González, E.; González-Calbet, J.M. Phase coexistence in $NaNb_{(1−x)}Ta_xO_3$ materials with enhanced dielectric properties. *J. Mater. Chem.* **2012**, *22*, 14938–14943.

47. Koruza, J.; Malič, B.; Kosec, M. Microstructure evolution during sintering of sodium niobate. *J. Am. Ceram. Soc.* **2011**, *94*, 4174–4178.

48. Manan, A.; Rehman, M.U.; Ullah, A.; Ahmad, A.S.; Iqbal, Y.; Qazi, I.; Khan, M.A.; Shah, H.U.; Wazir, A.H. High energy storage density with ultra-high efficiency and fast charging–discharging capability of sodium bismuth niobate lead-free ceramics. *J. Adv. Dielectr.* **2021**, *11*, 2150018.

49. Gao, P.; Liu, Z.; Zhang, N.; Wu, H.; Bokov, A.A.; Ren, W.; Ye, Z.-G. New antiferroelectric perovskite system with ultrahigh energy-storage performance at low electric field. *Chem. Mater.* **2019**, *31*, 979–990.

50. Chauhan, A.; Patel, S.; Vaish, R.; Bowen, C.R. Anti-ferroelectric ceramics for high energy density capacitors. *Materials* **2015**, *8*, 8009–8031.

51. Setter, N. What is a ferroelectric—A materials designer perspective. *Ferroelectrics* **2016**, *500*, 164–182.

52. Berlincourt, D. Transducers using forced transitions between ferroelectric and antiferroelectric states. *IEEE Trans. Sonics Ultrason* **1966**, *13*, 116–124.

53. Berlincourt, D.; Krueger, H.; Jaffe, B. Stability of phases in modified lead zirconate with variation in pressure, electric field, temperature and composition. *J. Phys. Chem. Solids* **1964**, *25*, 659–674.

54. Wei, X.-K.; Dunin-Borkowski, R.E.; Mayer, J. Structural phase transition and in-situ energy storage pathway in nonpolar materials: A review. *Materials* **2021**, *14*, 7854.

55. Zhang, H.; Wei, T.; Zhang, Q.; Ma, W.; Fan, P.; Salamon, D.; Zhang, S.-T.; Nan, B.; Tan, H.; Ye, Z.-G. A review on the development of lead-free ferroelectric energy-storage ceramics and multilayer capacitors. *J. Mater. Chem. C* **2020**, *8*, 16648–16667.

56. Yang, Z.; Du, H.; Jin, L.; Poelman, D. High-performance lead-free bulk ceramics for electrical energy storage applications: Design strategies and challenges. *J. Mater. Chem. A* **2021**, *9*, 18026–18085.

57. Engel, G.F. Design and materials of antiferroelectric capacitors for high density power electronic applications. In Proceedings of the CIPS 2016; 9th International Conference on Integrated Power Electronics Systems, Nuremberg, Germany, 8–10 March 2016; pp. 1–7.

58. Hao, X.; Zhai, J.; Kong, L.B.; Xu, Z. A comprehensive review on the progress of lead zirconate-based antiferroelectric materials. *Prog. Mater. Sci.* **2014**, *63*, 1–57.

59. Tan, X.; Ma, C.; Frederick, J.; Beckman, S.; Webber, K.G. The antiferroelectric↔ferroelectric phase transition in lead-containing and lead-free perovskite ceramics. *J. Am. Ceram. Soc.* **2011**, *94*, 4091–4107.

60. Zhou, Z.; Yang, Q.; Liu, M.; Zhang, Z.; Zhang, X.; Sun, D.; Nan, T.; Sun, N.; Chen, X. Antiferroelectric materials, applications and recent progress on multiferroic heterostructures. *Spin* **2015**, *5*, 1530001.

61. Chen, B.; Hasegawa, T.; Ohta, H.; Katayama, T. Antiferroelectric-to-ferroelectric phase transition in hexagonal rare-earth iron oxides. *J. Mater. Chem. C* **2022**, *10*, 5621–5626.

62. Prosandeev, S.; Prokhorenko, S.; Nahas, Y.; Yang, Y.; Xu, C.; Grollier, J.; Talbayev, D.; Dkhil, B.; Bellaiche, L. Hidden phases with neuromorphic responses and highly enhanced piezoelectricity in an antiferroelectric prototype. *Phys. Rev. B* **2022**, *105*, L100101.

63. Goh, Y.; Hwang, J.; Jeon, S. Excellent reliability and high-speed antiferroelectric $HfZrO_2$ tunnel junction by a high-pressure annealing process and built-in bias engineering. *ACS Appl. Mater. Interfaces* **2020**, *12*, 57539–57546.

64. Ali, T.; Mertens, K.; Olivo, R.; Rudolph, M.; Oehler, S.; Kühnel, K.; Lehninger, D.; Müller, F.; Hoffmann, R.; Schramm, P. Impact of the Nonlinear Dielectric Hysteresis Properties of a Charge Trap Layer in a Novel Hybrid High-Speed and Low-Power Ferroelectric or Antiferroelectric HSO/HZO Boosted Charge Trap Memory. *IEEE Trans. Electron Devices* **2021**, *68*, 2098–2106.

65. Müller, J.; Polakowski, P.; Mueller, S.; Mikolajick, T. Ferroelectric hafnium oxide based materials and devices: Assessment of current status and future prospects. *ECS J. Solid State Sci. Technol.* **2015**, *4*, N30.

66. Ali, F.; Abbas, A.; Wu, G.; Daaim, M.; Akhtar, A.; Kim, K.H.; Yang, B. Novel Fluorite-Structured Materials for Solid-State Refrigeration. *Small* **2022**, *18*, 2200133.

67. Muller, J.; Boscke, T.S.; Schroder, U.; Mueller, S.; Brauhaus, D.; Bottger, U.; Frey, L.; Mikolajick, T. Ferroelectricity in simple binary ZrO_2 and HfO_2. *Nano Lett.* **2012**, *12*, 4318–4323.

68. Ali, F.; Zhou, D.; Ali, M.; Ali, H.W.; Daaim, M.; Khan, S.; Hussain, M.M.; Sun, N. Recent progress on energy-related applications of HfO_2-based ferroelectric and antiferroelectric materials. *ACS Appl. Electron. Mater.* **2020**, *2*, 2301–2317.

69. Randall, C.A.; Fan, Z.; Reaney, I.; Chen, L.Q.; Trolier-McKinstry, S. Antiferroelectrics: History, fundamentals, crystal chemistry, crystal structures, size effects, and applications. *J. Am. Ceram. Soc.* **2021**, *104*, 3775–3810.

70. Xu, H.; Guo, W.; Wang, J.; Ma, Y.; Han, S.; Liu, Y.; Lu, L.; Pan, X.; Luo, J.; Sun, Z. A metal-free molecular antiferroelectric material showing high phase transition temperatures and large electrocaloric effects. *J. Am. Chem. Soc.* **2021**, *143*, 14379–14385.

71. Kambale, K.; Mahajan, A.; Butee, S. Effect of grain size on the properties of ceramics. *Met. Powder Rep.* **2019**, *74*, 130–136.

72. Zhang, T.; Lei, Y.; Yin, J.; Du, J.; Yu, P. Effects of pores on dielectric breakdown of alumina ceramics under AC electric field. *Ceram. Int.* **2019**, *45*, 13951–13957.

73. Haddour, L.; Mesrati, N.; Goeuriot, D.; Tréheux, D. Relationships between microstructure, mechanical and dielectric properties of different alumina materials. *J. Eur. Ceram. Soc.* **2009**, *29*, 2747–2756.

74. Megaw, H.D. The seven phases of sodium niobate. *Ferroelectrics* **1974**, *7*, 87–89.

75. Lefkowitz, I.; Łukaszewicz, K.; Megaw, H. The high-temperature phases of sodium niobate and the nature of transitions in pseudosymmetric structures. *Acta Crystallogr.* **1966**, *20*, 670–683.

76. Xu, Y.; Hong, W.; Feng, Y.; Tan, X. Antiferroelectricity induced by electric field in $NaNbO_3$-based lead-free ceramics. *Appl. Phys. Lett.* **2014**, *104*, 052903.

77. Mishra, S.; Choudhury, N.; Chaplot, S.; Krishna, P.; Mittal, R. Competing antiferroelectric and ferroelectric interactions in Na Nb O 3: Neutron diffraction and theoretical studies. *Phys. Rev. B* **2007**, *76*, 024110.

78. Lu, Z.; Sun, D.; Wang, G.; Zhao, J.; Zhang, B.; Wang, D.; Shyha, I. Energy storage properties in Nd-doped $AgNbTaO_3$ lead-free antiferroelectric ceramics with Nb-site vacancies. *J. Adv. Dielectr.* **2023**, *13*, 2242006.

79. Lu, Z.; Zhu, Y.; Sun, D.; Wang, B.; Wang, D.; Day, S.; Wang, G. Phases study for AgNb (Ta, W)O_3 lead-free antiferroelectric ceramics. *Results Eng.* **2023**, *20*, 101447.

80. Zhelnova, O.; Fesenko, O. Phase transitions and twinning in $NaNbO_3$ crystals. *Ferroelectrics* **1987**, *75*, 469–475.

81. Wood, E.; Miller, R.; Remeika, J. The field-induced ferroelectric phase of sodium niobate. *Acta Crystallogr.* **1962**, *15*, 1273–1279.

82. Cross, L.; Nicholson, B. LV. The optical and electrical properties of single crystals of sodium niobate. *Lond. Edinb. Dublin Philos. Mag. J. Sci.* **1955**, *46*, 453–466.

83. Ulinzheev, A.; Leiderman, A.; Smotrakov, V.; Topolov, V.Y.; Fesenko, O. Phase transitions induced in NaNbO$_3$ crystals by varying the direction of an external electric field. *Phys. Solid State* **1997**, *39*, 972–974.

84. Miller, R.C.; Wood, E.A.; Remeika, J.P.; Savage, A. Na (Nb$_{1-x}$V$_x$) O$_3$ System and "Ferrielectricity". *J. Appl. Phys.* **1962**, *33*, 1623–1630.

85. Cross, L. Electric double hysteresis in (K$_x$Na$_{1-x}$)NbO$_3$ single crystals. *Nature* **1958**, *181*, 178–179.

86. Luo, N.; Ma, L.; Luo, G.; Xu, C.; Rao, L.; Chen, Z.; Cen, Z.; Feng, Q.; Chen, X.; Toyohisa, F. Well-defined double hysteresis loop in NaNbO$_3$ antiferroelectrics. *Nat. Commun.* **2023**, *14*, 1776.

87. Chao, L.; Hou, Y.; Zheng, M.; Zhu, M. High dense structure boosts stability of antiferroelectric phase of NaNbO$_3$ polycrystalline ceramics. *Appl. Phys. Lett.* **2016**, *108*, 212902.

88. Dungan, R.; Golding, R. Metastable ferroelectric sodium niobate. *J. Am. Ceram. Soc.* **1964**, *47*, 73–76.

89. Li, W.; Xia, X.; Zeng, J.; Zheng, L.; Li, G. Significant differences in NaNbO$_3$ ceramics fabricated using Nb$_2$O$_5$ precursors with various crystal structures. *Ceram. Int.* **2020**, *46*, 3759–3766.

90. Koruza, J.; Groszewicz, P.; Breitzke, H.; Buntkowsky, G.; Rojac, T.; Malič, B. Grain-size-induced ferroelectricity in NaNbO$_3$. *Acta Mater.* **2017**, *126*, 77–85.

91. Fan, Y.; Zhou, Z.; Liang, R.; Zhou, M.; Dong, X. The effect of A-site nonstoichiometry on the microstructure, electric properties, and phase stability of NaNbO$_3$ polycrystalline ceramics. *J. Eur. Ceram. Soc.* **2019**, *39*, 4712–4718.

92. Zhang, M.-H.; Fulanović, L.; Egert, S.; Ding, H.; Groszewicz, P.B.; Kleebe, H.-J.; Molina-Luna, L.; Koruza, J. Electric-field-induced antiferroelectric to ferroelectric phase transition in polycrystalline NaNbO$_3$. *Acta Mater.* **2020**, *200*, 127–135.

93. Johnston, K.E.; Griffin, J.M.; Walton, R.I.; Dawson, D.M.; Lightfoot, P.; Ashbrook, S.E. 93Nb NMR and DFT investigation of the polymorphs of NaNbO$_3$. *Phys. Chem. Chem. Phys.* **2011**, *13*, 7565–7576.

94. Guo, H.; Shimizu, H.; Mizuno, Y.; Randall, C.A. Strategy for stabilization of the antiferroelectric phase (Pbma) over the metastable ferroelectric phase (P21ma) to establish double loop hysteresis in lead-free (1 − x) NaNbO$_3$-xSrZrO$_3$ solid solution. *J. Appl. Phys.* **2015**, *117*, 214103 .

95. Shimizu, H.; Guo, H.; Reyes-Lillo, S.E.; Mizuno, Y.; Rabe, K.M.; Randall, C.A. Lead-free antiferroelectric: X CaZrO$_3$-(1 − x) NaNbO$_3$ system (0 ≤ x ≤ 0.10). *Dalton Trans.* **2015**, *44*, 10763–10772.

96. Guo, H.; Shimizu, H.; Randall, C.A. Direct evidence of an incommensurate phase in NaNbO$_3$ and its implication in NaNbO$_3$-based lead-free antiferroelectrics. *Appl. Phys. Lett.* **2015**, *107*, 112904.

97. Shakhovoy, R.; Raevskaya, S.; Shakhovaya, L.; Suzdalev, A.D.; Raevski, I.; Yuzyuk, Y.I.; Semenchev, A.; El Marssi, M. Ferroelectric Q and antiferroelectric P phases' coexistence and local phase transitions in oxygen-deficient NaNbO$_3$ single crystal: Micro-Raman, dielectric and dilatometric studies. *J. Raman Spectrosc.* **2012**, *43*, 1141–1145.

98. Qi, H.; Zuo, R.; Xie, A.; Fu, J.; Zhang, D. Excellent energy-storage properties of NaNbO$_3$-based lead-free antiferroelectric orthorhombic P-phase (Pbma) ceramics with repeatable double polarization-field loops. *J. Eur. Ceram. Soc.* **2019**, *39*, 3703–3709.

99. Ma, L.; Chen, Z.; Luo, G.; Che, Z.; Xu, C.; Shan, D.; Cen, Z.; Feng, Q.; Chen, X.; Fujita, T. High energy storage density in NaNbO$_3$ antiferroelectrics with double hysteresis loop. *J. Mater.* **2023**, *in press*. https://doi.org/10.1016/j.jmat.2023.11.003.

100. Zhang, M.-H.; Ding, H.; Egert, S.; Zhao, C.; Villa, L.; Fulanović, L.; Groszewicz, P.B.; Buntkowsky, G.; Kleebe, H.-J.; Albe, K. Tailoring high-energy storage NaNbO$_3$-based materials from antiferroelectric to relaxor states. *Nat. Commun.* **2023**, *14*, 1525.

101. Kondo, N.; Sakamoto, W.; Lee, B.-Y.; Iijima, T.; Kumagai, J.; Moriya, M.; Yogo, T. Improvement in ferroelectric properties of chemically synthesized lead-free piezoelectric (K, Na)(Nb, Ta)O$_3$ thin films by Mn doping. *Jpn. J. Appl. Phys.* **2010**, *49*, 09MA04.

102. Guo, Y.; Xiao, P.; Wen, R.; Wan, Y.; Zheng, Q.; Shi, D.; Lam, K.H.; Liu, M.; Lin, D. Critical roles of Mn-ions in enhancing the insulation, piezoelectricity and multiferroicity of BiFeO$_3$-based lead-free high temperature ceramics. *J. Mater. Chem. C* **2015**, *3*, 5811–5824.

103. Wechsler, B.; Klein, M.B. Thermodynamic point defect model of barium titanate and application to the photorefractive effect. *JOSA B* **1988**, *5*, 1711–1723.

104. Ding, H.; Zhang, M.H.; Koruza, J.; Molina-Luna, L.; Kleebe, H.J. Domain morphology of newly designed lead-free antiferroelectric NaNbO$_3$-SrSnO$_3$ ceramics. *J. Am. Ceram. Soc.* **2021**, *104*, 3715–3725.

105. Villa, L.; Albe, K. Role of doping and defect quenching in antiferroelectric NaNbO$_3$ from first principles. *Phys. Rev. B* **2022**, *106*, 134101.

106. Berlincourt, D. Transducer using the electric field-forced antiferroelectric-ferroelectric transition. *Ultrasonics* **1968**, *6*, 48–51.

107. Zhou, M.; Liang, R.; Zhou, Z.; Dong, X. Superior energy storage properties and excellent stability of novel NaNbO$_3$-based lead-free ceramics with A-site vacancy obtained via a Bi$_2$O$_3$ substitution strategy. *J. Mater. Chem. A* **2018**, *6*, 17896–17904.

108. Yang, L.; Kong, X.; Li, Q.; Lin, Y.-h.; Zhang, S.; Nan, C.-w. Excellent energy storage properties achieved in sodium niobate-based relaxor ceramics through doping tantalum. *ACS Appl. Mater. Interfaces* **2022**, *14*, 32218–32226.

109. Kobayashi, K.; Ryu, M.; Doshida, Y.; Mizuno, Y.; Randall, C.A. Novel High-Temperature Antiferroelectric-Based Dielectric NaNbO$_3$–NaTaO$_3$ Solid Solutions Processed in Low Oxygen Partial Pressures. *J. Am. Ceram. Soc.* **2013**, *96*, 531–537.

110. Yadav, A.; Fahad, M.; Satapathy, S.; Sarun, P. Effect of tantalum on the temperature dependent electrical characteristics of NaNb1 − xTaxO$_3$ (0.0 ≤ x ≤ 0.3) ceramics between 400 and 560 °C. *J. Alloys Compd.* **2019**, *797*, 902–911.

111. Zhu, L.-F.; Yan, Y.; Leng, H.; Li, X.; Cheng, L.-Q.; Priya, S. Energy-storage performance of NaNbO$_3$ based multilayered capacitors. *J. Mater. Chem. C* **2021**, *9*, 7950–7957.

112. Chen, H.; Chen, X.; Shi, J.; Sun, C.; Dong, X.; Pang, F.; Zhou, H. Achieving ultrahigh energy storage density in NaNbO$_3$–Bi (Ni$_{0.5}$Zr$_{0.5}$)O$_3$ solid solution by enhancing the breakdown electric field. *Ceram. Int.* **2020**, *46*, 28407–28413.

113. Liang, C.; Wang, C.; Zhao, H.; Cao, W.; Huang, X.; Wang, C. Enhanced energy storage performance of NaNbO$_3$-based ceramics via band and domain engineering. *Ceram. Int.* **2023**, *49*, 40326–40335.

114. Liu, G.; Chen, L.; Qi, H. Energy storage properties of NaNbO$_3$-based lead-free superparaelectrics with large antiferrodistortion. *Microstructures* **2023**, *3*, 2023009.

115. Liu, J.; Li, P.; Li, C.; Bai, W.; Wu, S.; Zheng, P.; Zhang, J.; Zhai, J. Synergy of a stabilized antiferroelectric phase and domain engineering boosting the energy storage performance of NaNbO$_3$-based relaxor antiferroelectric ceramics. *ACS Appl. Mater. Interfaces* **2022**, *14*, 17662–17673.

116. Chen, H.; Wang, X.; Dong, X.; Pan, Y.; Wang, J.; Deng, L.; Dong, Q.; Zhang, H.; Zhou, H.; Chen, X. Adjusting the energy-storage characteristics of 0.95NaNbO$_3$–0.05Bi(Mg$_{0.5}$Sn$_{0.5}$)O$_3$ ceramics by doping linear perovskite materials. *ACS Appl. Mater. Interfaces* **2022**, *14*, 25609–25619.

117. Zhang, S.; Li, W.; Zhang, Y.; Tang, X.; Jiang, Y.; Guo, X. Excellent energy density and power density achieved in NaNbO$_3$-based relaxor ferroelectric ceramics. *Mater. Sci. Eng. B* **2024**, *299*, 117025.

118. Yang, W.; Zeng, H.; Yan, F.; Qian, J.; Zhu, K.; Zhao, K.; Li, G.; Zhai, J. Microstructure-driven excellent energy storage NaNbO$_3$-based lead-free ceramics. *Ceram. Int.* **2022**, *48*, 37476–37482.

119. Qi, H.; Li, W.; Wang, L.; Chen, L.; Liu, H.; Deng, S.; Chen, J. Large (anti) ferrodistortive NaNbO$_3$-based lead-free relaxors: Polar nanoregions embedded in ordered oxygen octahedral tilt matrix. *Mater. Today* **2022**, *60*, 91–97.

120. Wang, X.; Chen, H.; Pan, Y.; Dong, Q.; Wang, J.; Chen, X.; Zhou, H. Dielectric ceramics with excellent energy storage properties were obtained by doping 0.92NaNbO$_3$-0.08Bi (Ni$_{0.5}$Zr$_{0.5}$)O$_3$ ceramics. *J. Power Sources* **2023**, *566*, 232934.

121. Xie, A.; Zuo, R.; Qiao, Z.; Fu, Z.; Hu, T.; Fei, L. NaNbO$_3$-(Bi$_{0.5}$Li$_{0.5}$)TiO$_3$ lead-free relaxor ferroelectric capacitors with superior energy-storage performances via multiple synergistic design. *Adv. Energy Mater.* **2021**, *11*, 2101378.

122. Li, H.; Pan, Z.; Chen, X.; Zhao, J.; Tang, L.; Liu, J.; Li, P.; Zhai, J. Stable relaxor ferroelectric phase of NaNbO$_3$-based ceramic with superb energy storage performances. *Mater. Today Phys.* **2023**, *38*, 101208.

123. Qi, H.; Zuo, R.; Xie, A.; Tian, A.; Fu, J.; Zhang, Y.; Zhang, S. Ultrahigh Energy-Storage Density in NaNbO$_3$-Based Lead-Free Relaxor Antiferroelectric Ceramics with Nanoscale Domains. *Adv. Funct. Mater.* **2019**, *29*, 1903877. https://doi.org/10.1002/adfm.201903877.

124. Lv, Z.; Lu, T.; Liu, Z.; Hu, T.; Hong, Z.; Guo, S.; Xu, Z.; Song, Y.; Chen, Y.; Zhao, X. NaNbO$_3$-Based Multilayer Ceramic Capacitors with Ultrahigh Energy Storage Performance. *Adv. Energy Mater.* **2024**, *14*, 2304291.

125. Jiang, J.; Li, X.; Li, L.; Guo, S.; Zhang, J.; Wang, J.; Zhu, H.; Wang, Y.; Zhang, S.-T. Novel lead-free NaNbO$_3$-based relaxor antiferroelectric ceramics with ultrahigh energy storage density and high efficiency. *J. Mater.* **2022**, *8*, 295–301.

126. Jiang, J.; Meng, X.; Li, L.; Guo, S.; Huang, M.; Zhang, J.; Wang, J.; Hao, X.; Zhu, H.; Zhang, S.-T. Ultrahigh energy storage density in lead-free relaxor antiferroelectric ceramics via domain engineering. *Energy Storage Mater.* **2021**, *43*, 383–390. https://doi.org/10.1016/j.ensm.2021.09.018.

127. Liu, X.; Li, Y.; Sun, N.; Hao, X. High energy-storage performance of PLZS antiferroelectric multilayer ceramic capacitors. *Inorg. Chem. Front.* **2020**, *7*, 756–764. https://doi.org/10.1039/c9qi01416k.

128. Liu, X.; Li, Y.; Hao, X. Ultra-high energy-storage density and fast discharge speed of (Pb$_{0.98-x}$La$_{0.02}$Sr$_x$)(Zr$_{0.9}$Sn$_{0.1}$)0.995O$_3$ antiferroelectric ceramics prepared via the tape-casting method. *J. Mater. Chem. A* **2019**, *7*, 11858–11866. https://doi.org/10.1039/c9ta02149c.

129. Feng, Y.; Zhen, Y.; Jiang, X.; Yang, Z.; Qin, Z.; Yang, W.; Qie, Y.; Geng, H. Optimized energy storage performance in NaNbO$_3$-based ceramics via composition modification and micro-structure control. *Ceram. Int.* **2023**, *49*, 14135–14144.

130. Jiang, J.; Meng, X.; Li, L.; Zhang, J.; Guo, S.; Wang, J.; Hao, X.; Zhu, H.; Zhang, S.-T. Enhanced energy storage properties of lead-free NaNbO$_3$-based ceramics via A/B-site substitution. *Chem. Eng. J.* **2021**, *422*, 130130.

131. Qiao, Z.; Li, T.; Qi, H.; Zuo, R. Excellent energy storage properties in NaNbO$_3$-based lead-free ceramics by modulating antiferrodistortive of P phase. *J. Alloys Compd.* **2022**, *898*, 162934.

132. Yang, J.; Zhao, Y.; Zhu, L.; Hao, X. Enhanced electrocaloric effect of relaxor potassium sodium niobate lead-free ceramic via multilayer structure. *Scr. Mater.* **2021**, *193*, 97–102.

133. Jenko, D.; Benčan, A.; Malič, B.; Holc, J.; Kosec, M. Electron microscopy studies of potassium sodium niobate ceramics. *Microsc. Microanal.* **2005**, *11*, 572–580.

134. Zhang, T.; Karaki, T.; Fujii, T. The preparation of MnO$_2$-doped NaNbO$_3$-based lead-free ceramics with enhanced energy storage performance and attractive electrocaloric effect. *Jpn. J. Appl. Phys.* **2022**, *61*, SB1028.

135. Pan, Z.; Liu, B.; Zhai, J.; Yao, L.; Yang, K.; Shen, B. NaNbO$_3$ two-dimensional platelets induced highly energy storage density in trilayered architecture composites. *Nano Energy* **2017**, *40*, 587–595.

136. Lanfredi, S.; Dessemond, L.; Rodrigues, A.C. Effect of porosity on the electrical properties of polycrystalline sodium niobate: I, electrical conductivity. *J. Am. Ceram. Soc.* **2003**, *86*, 291–298.

137. Lanfredi, S.; Rodrigues, A. Impedance spectroscopy study of the electrical conductivity and dielectric constant of polycrystalline LiNbO$_3$. *J. Appl. Phys.* **1999**, *86*, 2215–2219.

138. Lanfredi, S.; Carvalho, J.; Hernandes, A.C. Electric and dielectric properties of Bi$_{12}$TiO$_{20}$ single crystals. *J. Appl. Phys.* **2000**, *88*, 283–287.

139. Harttar, M.A.M.; Rashid, M.W.A.; Azlan, U.A.A. Physical and electrical properties enhancement of rare-earth doped-potassium sodium niobate (KNN): A review. *Ceram. –Silikáty* **2015**, *59*, 158–163.

140. Lanfredi, S.; Rodrigues, A.C.; Dessemond, L. Effect of porosity on the electrical properties of polycrystalline sodium niobate: II, dielectric behavior. *J. Am. Ceram. Soc.* **2003**, *86*, 2103–2110.

141. Lu, Z.; Wang, G.; Bao, W.; Li, J.; Li, L.; Mostaed, A.; Yang, H.; Ji, H.; Li, D.; Feteira, A. Superior energy density through tailored dopant strategies in multilayer ceramic capacitors. *Energy Environ. Sci.* **2020**, *13*, 2938–2948.

142. Wang, G.; Li, J.; Zhang, X.; Fan, Z.; Yang, F.; Feteira, A.; Zhou, D.; Sinclair, D.C.; Ma, T.; Tan, X. Ultrahigh energy storage density lead-free multilayers by controlled electrical homogeneity. *Energy Environ. Sci.* **2019**, *12*, 582–588.

143. Qi, H.; Zuo, R. Linear-like lead-free relaxor antiferroelectric $(Bi_{0.5}Na_{0.5})TiO_3$–$NaNbO_3$ with giant energy-storage density/efficiency and super stability against temperature and frequency. *J. Mater. Chem. A* **2019**, *7*, 3971–3978.

144. Dong, X.; Li, X.; Chen, X.; Chen, H.; Sun, C.; Shi, J.; Pang, F.; Zhou, H. High energy storage density and power density achieved simultaneously in $NaNbO_3$-based lead-free ceramics via antiferroelectricity enhancement. *J. Mater.* **2021**, *7*, 629–639.

145. Tao, H.; Yin, J.; Zhao, C.; Wu, J. Relaxor behavior of potassium sodium niobate ceramics by domain evolution. *J. Eur. Ceram. Soc.* **2021**, *41*, 335–343.

146. Li, F.; Zhang, S.; Damjanovic, D.; Chen, L.Q.; Shrout, T.R. Local structural heterogeneity and electromechanical responses of ferroelectrics: Learning from relaxor ferroelectrics. *Adv. Funct. Mater.* **2018**, *28*, 1801504.

147. Yao, F.Z.; Wang, K.; Jo, W.; Webber, K.G.; Comyn, T.P.; Ding, J.X.; Xu, B.; Cheng, L.Q.; Zheng, M.P.; Hou, Y.D. Diffused phase transition boosts thermal stability of high-performance lead-free piezoelectrics. *Adv. Funct. Mater.* **2016**, *26*, 1217–1224.

148. Zhao, C.; Wu, B.; Wang, K.; Li, J.-F.; Xiao, D.; Zhu, J.; Wu, J. Practical high strain with superior temperature stability in lead-free piezoceramics through domain engineering. *J. Mater. Chem. A* **2018**, *6*, 23736–23745.

149. Xu, K.; Li, J.; Lv, X.; Wu, J.; Zhang, X.; Xiao, D.; Zhu, J. Superior piezoelectric properties in potassium–sodium niobate lead-free ceramics. *Adv. Mater.* **2016**, *28*, 8519–8523.

150. Zheng, T.; Wu, H.; Yuan, Y.; Lv, X.; Li, Q.; Men, T.; Zhao, C.; Xiao, D.; Wu, J.; Wang, K. The structural origin of enhanced piezoelectric performance and stability in lead free ceramics. *Energy Environ. Sci.* **2017**, *10*, 528–537.

151. Tao, H.; Wu, H.; Liu, Y.; Zhang, Y.; Wu, J.; Li, F.; Lyu, X.; Zhao, C.; Xiao, D.; Zhu, J. Ultrahigh performance in lead-free piezoceramics utilizing a relaxor slush polar state with multiphase coexistence. *J. Am. Chem. Soc.* **2019**, *141*, 13987–13994.

152. Koruza, J.; Liu, H.; Höfling, M.; Zhang, M.-H.; Veber, P. (K, Na) NbO_3-based piezoelectric single crystals: Growth methods, properties, and applications. *J. Mater. Res.* **2020**, *35*, 990–1016.

153. Liu, X.; Tan, X. Giant strains in non-textured $(Bi_{1/2}Na_{1/2})TiO_3$-based lead-free ceramics. *Adv. Mater.* **2016**, *28*, 574–578.

154. Machado, R.; Sepliarsky, M.; Stachiotti, M. Relative phase stability and lattice dynamics of $NaNbO_3$ from first-principles calculations. *Phys. Rev. B* **2011**, *84*, 134107.